CZECH TECHNICAL UNIVERSITY IN PRAGUE

Faculty of Nuclear Sciences and Physical Engineering

Department of Physics

Research project

Exclusive production at the LHC

Bc. Filip Nechanský

Supervisor: Mgr. Oldřich Kepka, Ph.D.

Prague, 2016

ČESKÉ VYSOKÉ UČENÍ TECHNICKÉ V PRAZE
FAKULTA JADERNÁ A FYZIKÁLNĚ INŽENÝRSKÁ
PRAHA 1 - STARÉ MĚSTO, BŘEHOVÁ 7 - PSČ 115 19

Katedra: fyziky **Akademický rok:** 2015/2016

VÝZKUMNÝ ÚKOL

Posluchač: Bc. Filip Nechanský

Obor: Experimentální jaderná a částicová fyzika

Vedoucí úkolu: Mgr. Oldřich Kepka, Ph.D., Fyzikální ústav, AV ČR, v.v.i.

Název úkolu (česky/anglicky): Exkluzivní produkce na LHC / Exclusive production at the LHC

Pokyny pro vypracování:

1. Seznanamte se s existujícími měřeními exkluzivní produkce na LHC.
2. Pomocí Monte-Carlo dat navrhněte měření dileptonové produkce pro těžišťovou energii 13 TeV.

Součástí zadání výzkumného úkolu je jeho uložení na webové stranky katedry fyziky.

Literatura:

[1] CMS Collaboration, Exclusive photon-photon production of muon pairs in proton-proton collisions at sqrt(s) = 7 TeV, JHEP 01 (2012) 052.

[2] CMS Collaboration, Study of exclusive two-photon production of W(+)W(-) in pp collisions at sqrt(s) = 7 TeV and constraints on anomalous quartic gauge couplings, JHEP 07 (2013) 116.

[3] ATLAS Collaboration, Measurement of exclusive $\gamma\gamma \rightarrow ll$ (l=e,μ) production in proton-proton collisions at sqrt(s) = 7 TeV with the ATLAS detector, Physics Letters B 749 (2015) 242-261.

[4] M. Dyndal, L. Schoeffel, The role of finite-size effects on the spectrum of equivalent photons in proton–proton collisions at the LHC, Physics Letters B, 741 (2015) 66-70.

Datum zadání: 23.10.2015 .....

Datum odevzdání: 24.06.2016 ***vedoucí katedry***

Prohlášení

Prohlašuji, že jsem svůj výzkumný úkol vypracovala samostatně a použila jsem pouze podklady (literaturu, software, atd.) uveřejněné v přiloženém seznamu.

Nemám závažný důvod proti užití tohoto školního díla ve smyslu §60 Zákona č.121/2000 Sb., o právu autorském, o právech souvisejících s právem autorským a o změně některých zákonů (autorský zákon).

V Praze dne 23.6.2016

Title:
Exclusive production at the LHC

Author: Filip Nechanský

Specialization: Experimental nuclear and particle physics

Sort of project: Research project

Supervisor: Mgr. Oldřich Kepka, Ph.D.

Abstract: In proton-proton collisions, quasi-real photons can be emitted and their interaction can produce various final states. However due to absorptive effects the exclusive cross-section is reduced. This decrease is described by survival factor, which has to be studied in order to properly model diphoton processes. The exclusive production of lepton pairs can be calculated in QED with small uncertainty and since only two back-to-back leptons are present in the final state, the process can be clearly distinguished from the background. This allows to compare the predicted and measured cross-section and dilepton production therefore serves as a standard candle for exclusive photon induced measurements. Here, such measurement is presented for case of two muons in final state at $\sqrt{s} = 13$ TeV, performed with ATLAS detector. The measured cross-section in defined fiducial region is found to be $\sigma_{excl} = 3.30 \pm 0.07(stat.) \pm 0.013(syst.)$pb.

Key words: exclusive diphoton processes, dilepton production, survival factor

Contents

List of Figures

Introduction

At the lower energy region, photons interact only with charged particles. Whether it is the photoelectric effect or pair production, we never observe photon interact with another photon. However, when we move to the high energy region, as e.g. at the LHC at CERN, we can observe such process. It is of course not direct interaction, since photon does not carry a electric charge, but is instead mediated by a charged propagator. One example of such process is in Figure 1, where the propagator is lepton and we can see two leptons in final state. This process is focus of the practical part of this thesis.

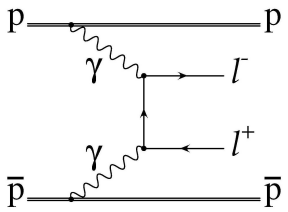

Figure 1: Feynman diagram of exclusive di-lepton production in proton-antiproton collision. Taken from [1].

The LHC does not collide high-energy photons, but protons. Nevertheless, due to the relativistic contractions the proton has significantly deformed electromagnetic field. The transverse component of such field can be interpreted as a quasi-real photon - a photon with low value of virtuality $Q^2 = -P_\gamma^2$.

Theoretical cross-section of a photon induced processes is reduced due to additional interactions between the colliding protons. The difference between the theoretical σ^{theory} and measured cross-section σ^{meas} is quantized by so-called survival factor S :

$$\sigma^{measured} = S \cdot \sigma^{theory} \tag{1}$$

Production of the dilepton pair has biggest yield from the diphoton processes and since it contains only two particles in the final state it is easily identifiable. Thus it can be used to study the survival factor and serves as standard candle of photon physics on LHC.

Study of this factor was done at 7 TeV on both ATLAS and CMS experiment and their results will be summarized later. Aside from new energies, current analysis plans to look into dependency of this factor on several kinematic variables, for example rapidity of the di-muon system or its mass.

Difficulty of this measurement comes from the low cross-section of the photon-induced processes. The dilepton final state is dominated by Drell-Yan process, which contribution must be reduced by carefully chosen selection.

Chapter 1

Theoretical overview

1.1 Standard model

Though not giving a final picture of the universe, the Standard Model of physics is best modern theory describing the fundamental forces and particles in the nature. It describes the three of the four fundamental forces - the strong, weak and electromagnetic force. Only the gravitational force is not implemented, though it is assumed to be carried by particle called graviton with spin 2. However this deficiency does not concern us since gravity is by far the weakest of the forces and can be neglected.

The standard model represents our best understanding of physics on the lowest scale, but it is known to be incomplete. For example it does not explain the mass of neutrinos or the dark matter. There are many theories trying to explain those problems, as for example Super Symmetry, but none of those have been experimentally confirmed.

1.1.1 Particles of the standard model

The elementary particles are divided between fermions with half-integer spin and bosons with integer spin. The elementary fermions are further split into two groups, quarks and leptons:

Quarks are particles which e.g. build-up the protons and neutrons - fundamental particles of the matter. They are divided in three generations and they have either charge +2/3 (up, strange and top quark) or -1/3 (down, charm and beauty), with the corresponding anti-particle partners. The up and down quarks are the lightest and are stable, unlike the heavier quarks which decay through weak interaction. Quarks are the only elementary particles which interact through all four forces.

Lepton also have three generations, each consisting of charged particle (electron, muon and tauon) and its corresponding neutrino. They interact through weak and electromagnetic interaction. Again, only the lightest electron is stable, while the two heavier lepton decay trough the weak force.

The elementary gauge bosons are representations of the three forces:

Photon carries the electromagnetic force. It has no mass, spin 1 and does not have a charge.

Gluons are responsible for the strong interaction. They carry the colour charge and can therefore self-interact. They are also massless.

Weak bosons are divided between one charged boson W^+ with its corresponding anti-particle W^- and one neutral boson Z. As their name suggest, the carry the weak force. Unlike the photons or gluons they are massive (they are one of the heaviest elementary particles).

Finally, the **Higgs boson** is particle responsible for the mass of elementary particles. Its discovery in 2012 marked a huge success of the standard model and the LHC project.

All the elementary particles are summarized in Figure 1.1.

Aside from the elementary particles, particle physics operates with composite particles. They are exclusively composed of quarks, either of three (with most known examples being proton and neutron)

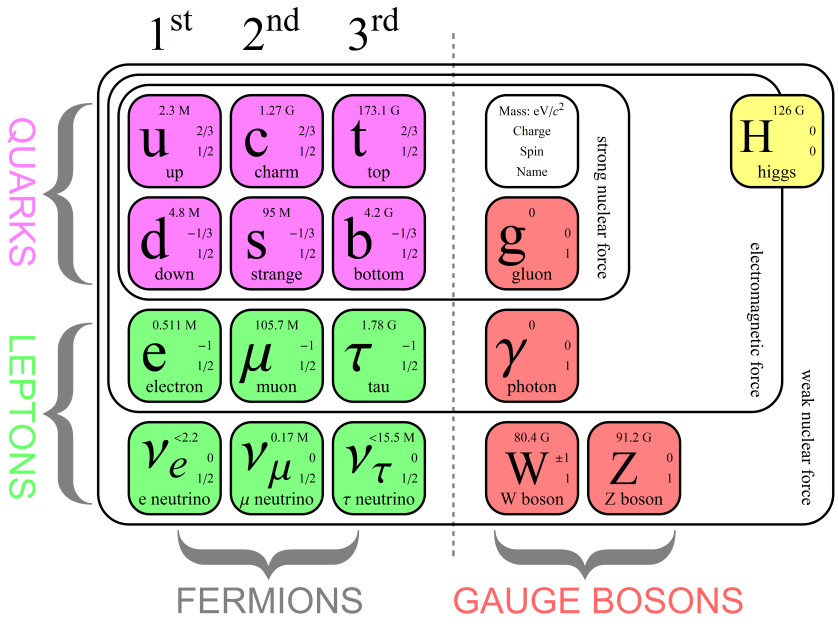

Figure 1.1: Particles of the standard model. Taken from [6].

or two (e.g. pion). There is strong evidence suggesting composite particle with four or five quarks, but this area is still not explored enough.

1.1.2 Quantum electrodynamics

Quantum electrodynamics (QED) is a quantum field theory of electromagnetic interaction - the interaction between charged particle. It has infinite range and is propagated by the masless photon. The QED lagrangian is:

$$\mathcal{L}_{QED} = \bar{\phi}(i\gamma^\mu \partial_\mu - m)\phi - \frac{1}{4} - q_e \bar{\phi}\gamma^\mu \phi A_\mu - \frac{1}{4} F^{\mu\nu} F_{\mu\nu},$$

where the first term is the Dirac Lagrangian of free 1/2-spin particle, second term describes the interaction of the particle with a photon and the last term is free electromagnetic field, with $F^{\mu\nu} = \partial^\mu A^\nu - \partial^\nu A^\mu$. Basic vertex of the QED is:

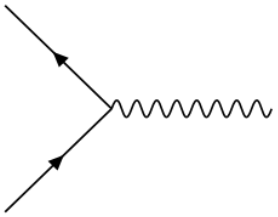

It can represent e.g. particle annihilation or emission of photon by particle. Even this simple vertex allows us to compute cross-section of the dilepton production in photon-photon collisions. It is important to note that there is no self interaction between photons in the QED.

Strength of an interaction is often connected with a value of coupling constant. For electromagnetic force in normal scale, the constant has value $\alpha_{em} = e^2/4\pi = 1/137$. Thought it is called constant, its

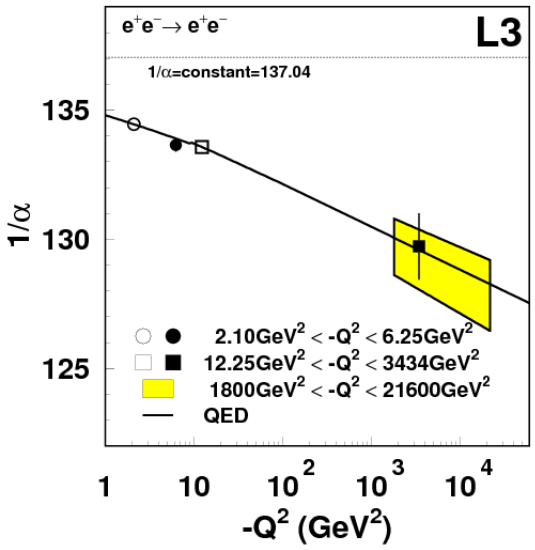

Figure 1.2: Comparison of predicted dependence of QED coupling constant on Q^2 and data acquired by LEP. Taken from [7].

value depends on scale in which we observe given process. The dependence on the virtuality Q^2[1] (or *renormalization scale*) is following:

$$\alpha_{em}(Q^2) = \frac{\alpha_{em}(m_e)}{1 - \Delta\alpha_{em}(Q^2)} \approx \frac{\alpha_{em}(m_e)}{1 - \frac{\alpha_{em}(m_e)}{3\pi}\log(\frac{Q^2}{m_e^2})}$$

in the first order of a perturbation theory. It diverges for $Q^2 \to \infty$. The dependence is caused by sea of virtual particles (primarily electron-positron pairs) surrounding the charged particle, effectively screening its charge. Higher the transferred momentum, the closer to the charge we are and smaller the screening is.

The scale dependence of the Quantum Electrodynamics was tested for example on the LEP experiment at CERN and shows excellent agreement between theory and data[7]. The results are in Figure 1.2.

1.1.3 Electro-weak theory

The weak force, as the name suggests, is the weakest of the forces of the standard model. It is also the only force concerning all of the elementary particles. Even though it has significantly different in strength and processes from the electromagnetic interaction, it was found that they can be united in the electro-weak theory, also known as *Glashow-Salam-Weinberg* model with $SU(2) \otimes U(1)$ symmetry.

The theory works with one boson triplet $W^{(1)}, W^{(2)}, W^{(3)}$ and one iso-scalar boson B_μ. By process of spontanus symmetry breaking through scalar higgs boson the triplet bosons gain mass - those are known as the charge $W^\pm$ and Z boson - and one masless photon A, where the Z and A are connected with the original wavefunction through Weinberg angle Θ_W:

$$Z = W^{(3)}\cos\Theta_W - B\sin\Theta_W, A = W^{(3)}\cos\Theta_W + B\sin\Theta_W$$

[1] Virtuality is an negative value of four-momentum P of particle squared: $Q^2 = -P^2$. More off-shell this value is, more virtual given particle is. It can be either time-like virtuality for $P^2 > m^2 \approx 0$ or space-like for $P^2 < m^2 \approx 0$.

while the charged W bosons are linear combination of the $W^{(1)}, W^{(2)}$:

$$W^+ = \frac{W^{(1)} - iW^{(2)}}{\sqrt{2}}, W^- = \frac{W^{(1)} + iW^{(2)}}{\sqrt{2}}$$

The Weinberg angle also connects the mass of Z and W bosons: $M_Z^2 \approx M_W^2 / \cos^2 \Theta_W$

There is a large number of processes connected with weak and electroweak interaction, however only three of them will be of particular interest to us:

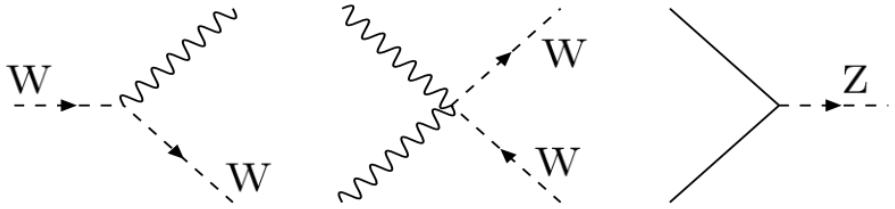

First is simple emission of photon by a charged W boson, second is anomalous quadratic vertex and third is annihilation of two fermions (leptons or quarks) to Z boson.

1.1.4 Quantum chromodynamics

Quantum Chromodynamics is the theory of strong interaction - interaction between quarks and gluons. Similarly to electrodynamics, strong force has a charge. More precisely it has three charges, called colours: red and anti-red ($R\bar{R}$), green and anti-green ($G\bar{G}$), and blue and anti-blue ($B\bar{B}$). Colour was first implemented as another degree of freedom, since Δ^{++} would have a symmetrical wave function even though it is a fermion. The number of colours was definitely determined from the ratio of cross-section of $e^+e^- \to q\bar{q}$ and $e^+e^- \to \mu^+\mu^-$ processes.

Lagrangian of QCD is based on SU(3) group[2]. Its 9 linearly independent elements can be divided between one singlet $\frac{1}{\sqrt{3}}(R\bar{R} + G\bar{G} + B\bar{B})$ invariant under SU(3) transformation and eight elements affected by such transformation. For this reason QCD has 8 generators - gluons - as carriers of the interactions. Unlike photons, the gluons carry a charge and therefore can emit additional gluons. This small detail has large consequences and it is the main reason why strong interaction is stronger at larger distances. The basic QCD vertices are:

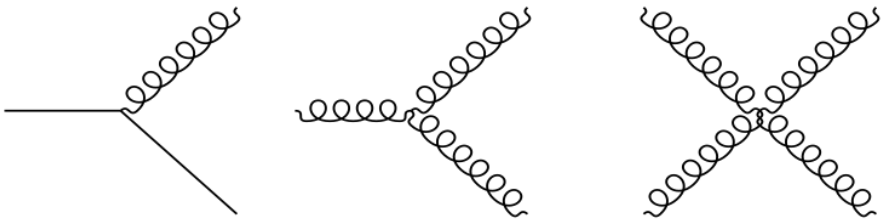

The first one is a simple gluon emission by a fermion (similarly to QED and emission of photon), while the second and third is self-interaction of three and four gluons - process not observed in the QED.

The QCD is also not scale-independent and coupling constant of strong interaction α_s changes as a function of Q^2 similarly to electromagnetic interaction. Nevertheless, here the similarity ends, since the dependence on the momentum transfer is opposite. QCD is strongest at low Q^2 as can be seen in Figure 1.3.

[2]Unitary 3x3 matrices with determinant equal to 1.

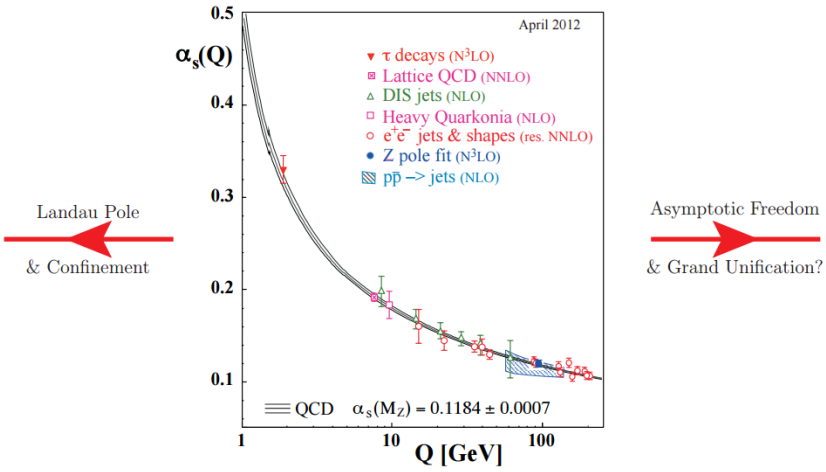

Figure 1.3: Dependence of coupling constant of strong interaction on Q^2. Taken from [8].

The fact that strength of the interaction increases with distance leads to a confinement - quarks are confined in baryons and mesons as colour singlets. For this reason colour cannot be observed directly in low energy experiments. On the other hand, when energy is high, force acting on quarks is weaker and they can move as if they were free. This is called asymptotic freedom. At energies around $10^{15} - 10^{17}$ GeV the strong interaction is as weak as the electromagnetic interaction. The fact that coupling constant can have low values enables usage of the perturbative quantum field theory in higher energy regions.

1.2 Classical photon interactions

First we shall review the classical photon interactions before delving into the more unusual photon-photon interaction:

Photoelectric absorption is a interaction of photon with electron shell of an atom. The photon is absorbed by the atomic shell, resulting in emission of electron. The threshold energy of such process is the binding energy of the electron(s) and the cross-section is proportional to $Z^n/E_\gamma^{3.5}$, where Z is atomic number, E_γ energy of the photon and n is 'constant', which value varies between 4 and 5[4].

Compton scattering from classical point of view is process when photon interacts with an electron, transferring part of its energy in the process. Quantum electrodynamics views this process as absorption of the photon by the electron followed by emission of new photon (Feynman diagram of this process is in Figure1.4). The energy of the out-going photon depends on the scattering angle λ: $E'_\gamma = \frac{m_e E_\gamma}{m_e + E_\gamma(1-\cos\theta)}$ and the cross-section is described by Klein-Nishina formula[5]:

$$\frac{\mathrm{d}\sigma}{\mathrm{d}\Omega} = \frac{\alpha^2}{2m_e^2}\left(\frac{E'_\gamma}{E_\gamma}\right)^2\left[\frac{E'_\gamma}{E_\gamma} + \frac{E_\gamma}{E'_\gamma} - \sin^2\theta\right]$$

Normally the scattered photon loses energy. However the opposite process where high energy electron transfers energy to the photon is also possible. It is called **inverse Compton scattering** and it will come back in latter section of this chapter, since it is convenient source of high energy photons.

The **pair production**, also known as the Bethe-Heitler process, has the same final state and also uses similar process to the exclusive dilepton production. The conservation laws forbid single photon

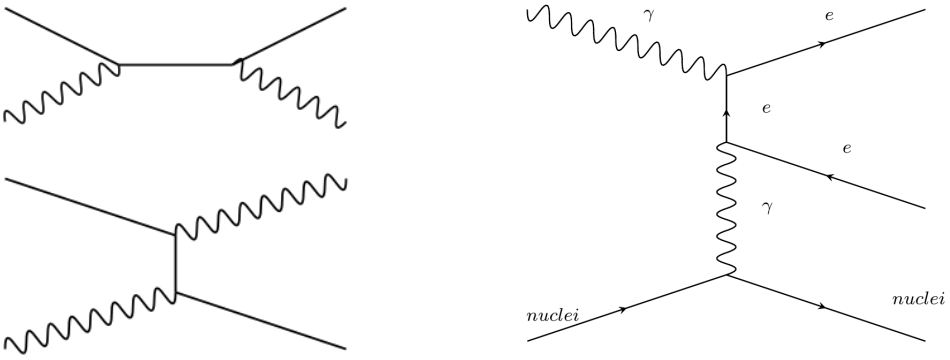

(a) (b)

Figure 1.4: (a) Feynman diagrams of Compton scattering. (b) Feynman diagram of pair production in proximity of a nucleus.

to decay into an electron-positron pair, however when another object (typically nuclei) is present, such process becomes possible. The Feynman diagram is in Figure 1.4. The only difference from the dilepton production is that one of the photons is not real, but virtual photon emitted by the nucleus.

There are many other common photon processes, but those are the most well known. All of those processes however have one mutual property - the photon always interacts with another charged particle. This is something we would expect, since photons do not carry electric charge and therefore cannot interact with each other through electromagnetic force. However in reality there are indeed interactions of two photons, with variety of final states.

1.3 Photon-photon interaction

Possibility of diphoton interactions was proposed as soon as in year 1934 in paper [9]. It described possibility of production of a electron-positron pair in photo-photon interactions. The proper theory however came much later with the QED and EW.

Diphoton processes were never observed by direct collision of two photons, but they can be measured in collisions of ultra-relativistic charged particles. This will be discussed in detail in next chapter. Here is review of the most important photon-photon processes:

1.3.1 Dilepton production

Dilepton production, in case of electrons called Breit-Wheeler pair production, is the most common of the photon induced processes. The feynman diagram was already presented in Figure 1. In the lowest order of the perturbation theory the cross-section of dilepton production takes form[11]:

$$\sigma^{\gamma\gamma\to l^+l^-} = \frac{4\pi\alpha^2}{s}\left[\left(1+\frac{4m_l^2}{s}-\frac{8m_l^4}{s^2}2\ln\left(\frac{\sqrt{s}}{2m_l}+\sqrt{\frac{s}{4m_l^2}-1}\right)-\left(1+\frac{4m_l^2}{s}\right)\sqrt{1-\frac{4m_l^2}{s}}\right)\right]\Theta(s-4m_l^2),$$

where m_l is mass of the lepton (electron, muon or tauon) The s is the invariant mass of the system and is equal to invariant mass of the lepton pair, which will be denoted m_{ll} (variable which will be frequently used in later sections). The minimal energy of the system is - understandably - $\sqrt{s} = 2m_l$.

It was found[12], that the production of electron-positron pairs from two photons is responsible for cut-off in high energy gamma rays in cosmic rays. The absorbtion reaches maximum around 1 TeV. It is also responsible for production of electron pairs in gamma ray burst[13].

1.3.2 W^+W^- production

The exclusive diphoton production of two weak bosons can happen in three channels:

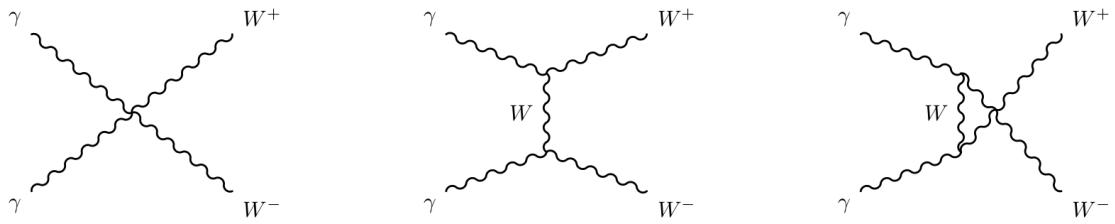

(a) QGC vertex (b) t-channel (c) u-channel

Especially the first one is the reason why is this process interesting, since it involves anomalous quadratic gauge and thus it can be used for investigation of the Standard model. The unpolarized cross-section (again in the Born approximation) is[14]:

$$\sigma_{\gamma\gamma\to W^+W^-} = \frac{6\pi\alpha^2}{s}\left[\beta\cos\theta_{cut} - 4\frac{M_2^2}{s}\left(1-\frac{2M_W^2}{s}\right)\log\left(\frac{1+\beta\cos\theta_{cut}}{1-\beta\cos\theta_{cut}}\right) + \left(\frac{1}{3}+\frac{M_W^4}{s^2}\right)\frac{16\beta\cos\theta_{cut}}{1-\beta^2\cos\theta_{cut}}\right],$$

where M_W is mass of the W boson, β is its velocity in center-of-mass system and θ is a scattering angle. As was the case for the dilepton production, there is a cut-off at $2m_W$ for the invariant mass of the dilepton system. For high invariant mass of the diphoton system the cross-section becomes almost constant:

$$\sigma_{\gamma\gamma\to W^+W^-} \to \frac{8\pi\alpha^2}{M_W^2} \approx 80pb$$

and it is dominant process at high energies. Corrections to the first order of perturbation theory are presented in the paper [14].

Analysis of this problem is problematic since the weak boson decays into additional particles. It is usually measured in a final state containing two leptons (often electron and muon in order to distinguish it from the dilepton processes). This process was studied on the CMS experiment at 7 TeV [15], analysis with ATLAS at 7 TeV is not yet published. An measurement at 13 TeV on ATLAS is also planned.

1.3.3 Light-by-light scattering

Perhaps the most counter-intuitive process is scattering of photon on photon. Since photons do not have a charge and therefore cannot interact directly, this process is only possible through a charged particle propagator. The most basic process of $\gamma\gamma$ scattering is through lepton box diagram:

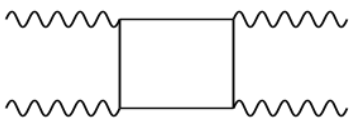

This process was not yet observed, even though there have been limits on the cross-section. E.g. for 0.8 ev photons it is $\sigma_{\gamma\gamma\to\gamma\gamma}$ <1.5·10^{-24} b. For this energy region the predicted cross-section is $7.3\cdot10^{-42}$ b[17, 18], so the result is still in agreement with Standard Model.

Measurement of this process is planned on the LHC, however the cross-section is small (12 fb, 26 pb, 35 nb in $p-p, p-Pb, Pb-Pb$ collision). This equals to around 20 signal events per run[16].

1.3.4 Additional photon-photon processes

Additional processes are e.g. production of quark pair (which does not have as clear background as the lepton production since the quarks must hadronize). Further there is double lepton pair production with following feynman diagram:

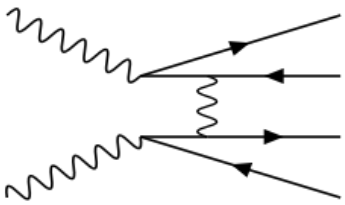

Important process is also exclusive production of the Higgs boson:

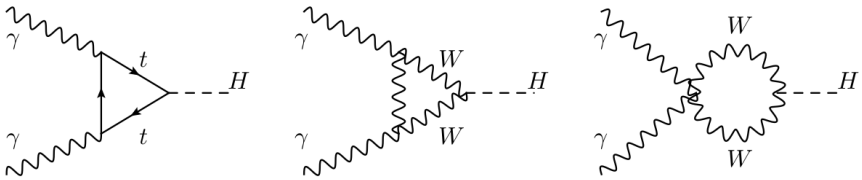

There are many other processes but those already mentioned are the most important.

1.3.5 Direct $\gamma\gamma \to e^+e^-$ measurement

As was already mentioned, there is no measurement of a direct diphoton interaction from collisions of photons. All current knowledge of this process comes from a collision of massive charged particles. Since the diphoton cross-section increases with an energy, such measurement of direct photon collision would require a high-energy high-intensity photon sources - something not available for a long time. However in recent years, two propositions for such analysis appeared, one combining high energy photons interacting with black body radiation[19] and second for collision of two laser beams[20].

Chapter 2

Dilepton production in collisions of charged particles

As was explained in previous chapter, it is technically difficult to realize a photon collider with sufficient energies and intensities to study a photon-photon interaction. However, collisions of charged particles offer a way to study such processes.

For electron collisions, the description was done by S. J. Brodsky [10]. In such case the photons are virtual. Even though the cross-section of those processes is rather low (mainly due to presence of a large number of photon vertices), it becomes comparable to cross-section of single photon processes in higher energy regions [10]. For hadrons the situation is more complicated since they have structure, but it is still powerful tool for investigation of photon-photon processes.

2.1 Equivalent Photon Approximation

An ultra-relativistic particles have deformed electromagnetic field - due to the relativistic contraction. Such field can be interpreted as quasi-real photons - photon with small virtuality (this concept is displayed in picture 2.1). When the particles - whether it is proton or nucleus - either collide or fly past each other, the photon fields can interact, in the same time leaving the colliding particles intact. This processes is more significant for heavy nuclei, since intensity of the fields (and therefore the equivalent photons) is proportional to the charge of the particle.

The motion of interpretation of the transverse field as photons is called *Equivalent photon approximation*, a method first proposed by E. Fermi [22] and further developed by C. F. v. Weizäcker and J. Williams [23, 24]. Given a cross-section of some diphoton induced process, e.g. dilepton production $\sigma_{\gamma\gamma\to l^+l^-}(m_{l^+l^-})$, a total cross-section of such process in collision of two nuclei A_1, A_2 can be written as[3]:

$$\sigma^{EPA}_{A_1A_2\to A_1A2l^+l^-} = \int\int P(x_1)P(x_2)\sigma_{\gamma\gamma\to l^+l^-}(m_{l^+l^-})\mathrm{d}x_1\mathrm{d}x_2,$$

where x_i are fractions of energy of the proton carried by the photons, P are photon distributions given by the EPA and $m_{l^+l^-}$ is invariant mass of the dilepton (and in same time of the diphoton) system. The mass is connected to the x_1, x_2 by simple formula $m^2_{l^+l^-} = x_1x_2s$, assuming there is no angle between the photon trajectories.

Such method can be applied to most of the diphoton induced processes, if the virtuality of the photons is small (which can be described by inequality $W_{\gamma\gamma} >> Q^2$)[21]. The low virtuality also means that the resulting leptons are emitted back-to-back.

It was found at the LHC (at energies $\sqrt{s} = 7TeV$ that average virtuality of photons is of order 0.01 GeV^2, satisfying this requirement for energies considered.

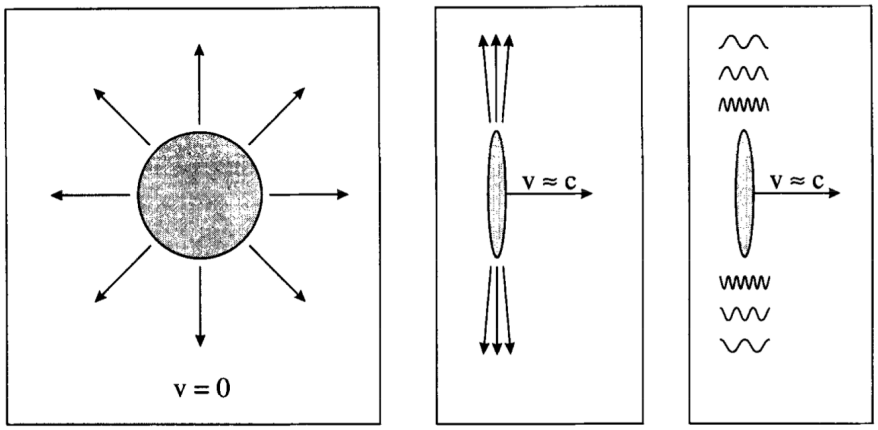

Figure 2.1: Sketch describing Fermi's idea of intepreting EM field of ultra-relativistic charged particles as swarm of photons. Taken from [22].

For elastic collision (where both protons survive the interaction) can the photon distribution function been written as [25]:

$$P_e(x) = \frac{\alpha}{\pi x}\int_{Q^2_{min}}^{Q^2_{max}} \frac{\mathrm{d}Q^2}{Q^2}\left[\left(1-\frac{Q^2_{min}}{Q^2}\right)(1-x)\,F_E(Q^2) + \frac{x^2/2}{2}F_M(Q^2)\right],$$

where $F_E(F_M)$ are electromagnetic structure functions of the proton.

Situation is further complicated by several factors. The electromagnetic field is the strongest in proximity of the nuclei and therefore close interaction of the protons will result in high-energy photon collisions. However when they are close enough to interact by the strong force, the diphoton production is obscured by additional processes. Furthermore, one or both nuclei may dissociate due to the photon interaction. Such thing requires further explanation and is important in order to properly analyze the dilepton process.

2.1.1 Impact parameter dependence

The dependence on the impact parameter is connected to term introduced in the introduction and that is survival factor. Survival factor takes in an account the fact, that aside from the exclusive production, additional proton-proton rescattering is possible. Even though the diphoton process is still present, it is impossible to identify it in the underlaying event background.

Given the low transfered momentum the survival factor is part of the soft QCD (QCD with low momentum transfers) and therefore cannot be computed through the perturbation theory. One of the most recent approaches is summarized in [26](Appendix A) and in more detail in [27]. Basic idea is to parametrize how is the amplitude of the process affected by the additional interaction.

First, consider the amplitude of the bare process in Figure 2.2a) $T(q_{1t}, q_{2,t})$. The rescattering amplitude (in Figure 2.2b)) can be that defined as $T^{res}(q_{1t}, q_{2t}) = \frac{i}{s}\int \frac{\mathrm{d}^2k_t}{8\pi^2} T_{el}(k_t^2) T(q_{1t}+k_t, q_{2t}-k_t)$. Combining these two amplitudes one gets the average survival factor[27]:

$$< S^2 >= \frac{\int \mathrm{d}^2q_{1t}\mathrm{d}^2q_{2t}|T(q_{1t},q_{2t}) + T^{res}(q_{1t},q_{2t})|^2}{\int \mathrm{d}^2q_{1t}\mathrm{d}^2q_{2t}|T(q_{1t},q_{2t})|^2}$$

This formula can be rewritten in terms of the impact parameters $\vec{b_{1t}}, \vec{b_{2t}}$ describing transverse separa-

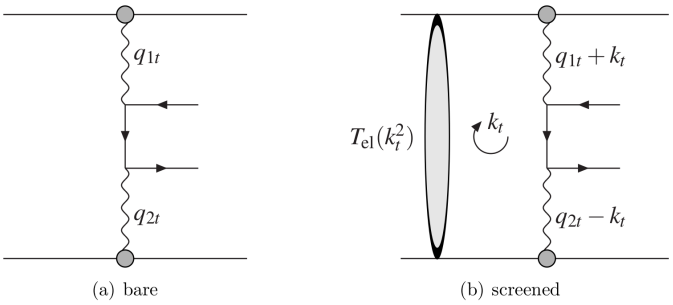

Figure 2.2: Feynman diagrams of dilepton production (a) without (b) with additional rescattering of the protons. Taken from [27].

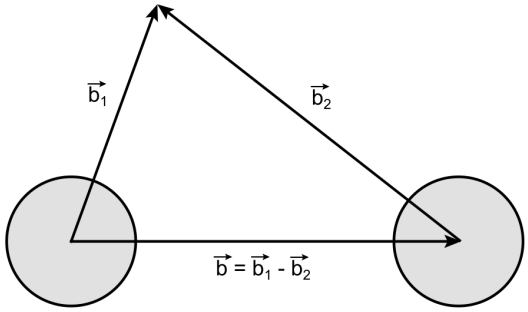

Figure 2.3: Definition of the impact parameter vectors. Taken from [21].

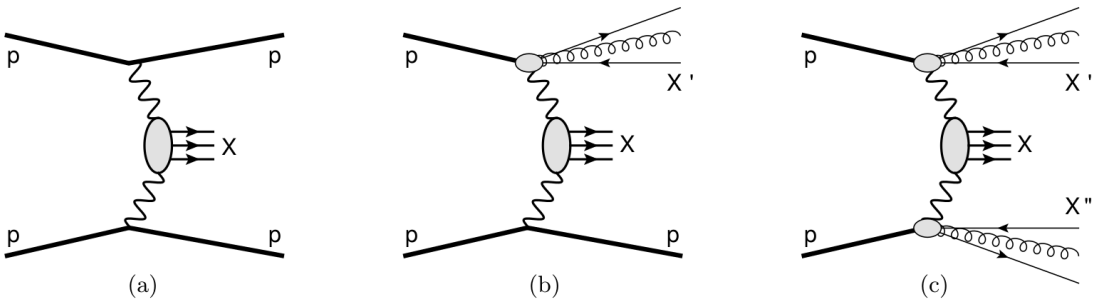

Figure 2.4: Diagrams showing the three basic types of diphoton production: (a) elastic,(b) single dissociative and (c) double dissociative. Taken from [21].

tion (vectors $\vec{b_1}, \vec{b_2}$ are visualized in Figure 2.3) and distance between the protons $b_T = |\vec{b_{1t}} - \vec{b_{2t}}|$[26]:

$$< S^2 >= \frac{\int \mathrm{d}^2\vec{b_{1t}}\mathrm{d}^2\vec{b_{2t}}|T(\vec{b_{1t}}, \vec{b_{2t}})|^2 \exp(-\Omega(s, b_t))}{\int \mathrm{d}^2\vec{b_{1t}}\mathrm{d}^2\vec{b_{2t}}|T(\vec{b_{1t}}, \vec{b_{2t}})|^2},$$

where $\Omega(s, b_t)$ is the proton opacity, which describes probability of no inelastic scattering. The suppression of the exclusive production is bigger with smaller distance between the protons - behavior one would expect.

In reality one cannot measure the impact factor, but it is still manifested in the dependence of the survival factor on other variables. Study of those dependences (aside from measurement of the average survival factor) is one of the motivations for this measurement.

2.1.2 Dissociative production

Even though the momentum transfers are usually small and proton emitting the photon is deflected in a small angle, it can sometimes dissociate into additional partons, as is shown in Figure 2.4, where either one or both protons break down. Thus we have three possible reactions: *exclusive* (or elastic), where both protons survive, *single dissociative* (SDiss), where one of the protons survives and finally *double dissociative* (DDiss)with both protons destroyed.

Since the dissociation is QCD processes, its computation is more complicated. It affects the final state leptons and therefore the dilepton spectra are significantly different that in the elastic case [28]. The dissociative components represent another non-negligible background. Since the partons from the dissociation are usually emitted in forward direction, they are often not detected and therefore such event cannot be differentiated from the exclusive production.

2.2 Previous measurements

The exclusive dilepton production was already studied on several experiment, e.g. on Tevatron for both electrons and muons on the CDF experiment[29, 30, 31], at HERA with the H1 detector[32] or at RHIC on experiments STAR[33] and PHENIX[34]. All analyses were in agreement with the standard model.

The survival factor was studied on ATLAS[3] and CMS[28] experiments at the LHC. Both measurements were at the 7 TeV in proton-proton collisions for muons, ATLAS also included the production of electron-positron pairs.

Both analyses used similar method to derive the survival factor and arrived to compatible results, which are displayed in Figure 2.5. The survival factor was found to be around 80%. The ATLAS

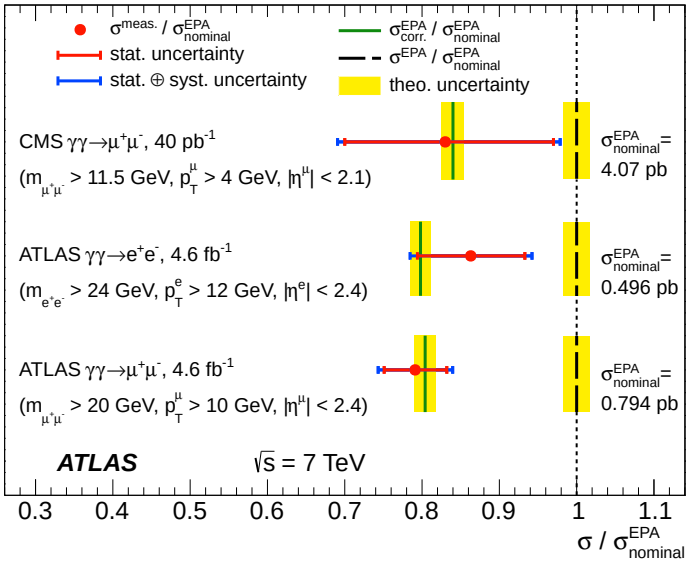

Figure 2.5: Survival factors derived in ATLAS and CMS for the dilepton production, compared to theoretical prediction. Taken from [3].

analysis served as inspiration for current 13 TeV measurement. Due to the better statistics during Run 2 on the LHC, much precise results are expected, allowing to study dependence of the survival factor on various kinematic observables.

2.3 Monte Carlo

2.3.1 Overview of generators

In order to study the exclusive processes, one has to have good idea about the distributions of processes with same final states. The dissociative components (SDiss and DDiss) were already mentioned. Additional background is e.g. production of tauon pairs, which cannnot be measured directly, but may decay into muons and electrons. Further, there is Drell-Yan contribution - two quarks annihilating into either Z or γ, which can further decay into either electron or muon pair. This process is dominant background in both ee and $\mu\mu$ channel and has significant peak at the mass of the Z boson. There is also contribution from processes containing two top quarks decaying into two leptons and QCD Multijet coming from mis-identification of $b\bar{b}$ and $c\bar{c}$ jets.

All background MC were already produced, while the diphoton processes had to be simulated, which was first task of the analysis.

The exclusive component is simulated using Herwig++ Monte Carlo generator. It uses the EPA formalism and does not include the survival factor. The dominant background is the **Single-dissociative dilepton** production, which is simulated using LPair MC. It uses Suri-Yenni and Brasse Fragmenation models, where for low Q^2 values, mostly low-multiplicity states are created together with products of Δ decay, while for the high Q^2 there is large number of various final states [3] through various resonances with large activity at forward regions. It also does not include the survival factor effects.

The double-dissociative background is generated using Pythia 8.212 with photon distribution functions NNPDF 2.3 QED, using LO, NLO and NNLO perturbative expansion, starting at $Q^2 = 2$ GeV. It uses default string fragmentation model of Pythia 8 and also includes absorptive effects, which

employ the default multi-parton model.

The Drell-Yan samples are generated using the PowHeg v2 generator and further interfaced with Pythia 8 to include parton showers. Finally, the $t\bar{t}$ processes are produced using the PowHeg with with CT10 PDF, using the Pythia 6 to simulate additional evolution of the system.

Pile-up is simulated using minimum bias events from Pythia, which is then reweighted to match data. The simulation of passage through the ATLAS detector is done in Geant 4.

2.3.2 Double-dissociative production

The double-dissociative production allows for various modifications and setting, whose effects had to be studied to determine the best configuration for the generation.

First test was whether the distributions are significantly affected by choice of the order of perturbative expansion. Pythia allows to use only the leading order, next-to-leading order and next-to-next-to-leading order. As can be seen from Figure 2.6 a), the difference can be quite significant and it is necessary to use the highest order available.

Pythia further allows to choose from three values of the strong constant $\alpha_s = 0.117, 0.118, 0.119$ (since dissociation is strong process and therefore is affected by such choice). Again, the effect is displayed in Figure 2.6 and is found to be smaller than $< 1\%$.

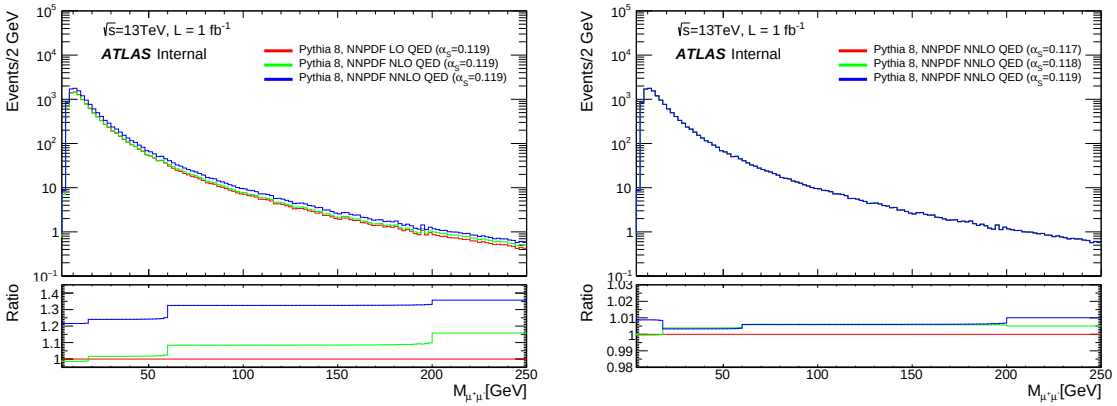

Figure 2.6: Comparison of $M_{\mu^+\mu^-}$ distributions, (a) for three different levels of perturbation order and (b) for three different values of α_s

Chapter 3

Experiment ATLAS

This chapter describes the experiment ATLAS, in which this measurement takes place, starting with description of the Large Hadron Collider, which supplies ATLAS with collisions, and ending with a description of individual sub-detectors.

3.1 Large Hadron Collider

Large Hadron Collider (LHC) is a circular proton-proton collider situated at CERN near Geneva, Switzerland. It collides protons with the largest center-of-mass energy in the world, with a maximal planned energy of 14 TeV and current energy of 13 TeV. The high energies enable to study problems on and beyond borders of modern science. For example in the year 2012 both the ATLAS and CMS, the general purpose experiments of the LHC, were able to confirm Higgs boson, a missing particle of the Standard Model [35]. Experiment ALICE on the other hand studies e.g. Quark Gluon Plasma, theorized state of matter present at earliest moments of the universe. The last experiment LHCb focuses on the study of b-hadrons and CP symmetry breaking.

The tunnel of the LHC is around 27 km long, with additional smaller accelerators providing injecting energy of 900 GeV[1]. There are approximately 2800 bunches at the same time along the ring, with approximately 10^{11} protons present in each bunch. Bunches flow through two separate magnetic channels, which only intersect in four places, where the four experiments are situated. Magnets need to be cooled down to -271.3°C, which is ensured by a large amount of a liquid helium. In order to minimize a loss of particles, an ultra-high vacuum must be created in the tubes with the beam particles. The protons currently collide $40 \cdot 10^6$ times per second. Number of colliding particles and the frequency of their collisions can be summed in luminosity, which is a proportionality factor between cross-section of some process and number of events in which this process occurred.

3.2 ATLAS detector overview

ATLAS, A Toroidal LHC Apparatus, is a cylindrical detector consisting of a main barrel and two discs (end-caps). It is 42 m long, has diameter of 22 meters and weights around 7000 tons. The detector consists of four main parts - Inner Detector, Electromagnetic Calorimeter, Hadronic Calorimeter and Muon Spectrometer. The Inner Detector is surrounded by a 2T solenoid superconducting magnet, with additional eight 0.5T super-conducting toroidal magnets placed symmetrically around the beam pipe and two additional 1T in the end-caps. Schematic view of the detector is in Figure (3.1).

Coordinates in the ATLAS are defined as follows: origin point is in the center of the detector with z axis parallel with the beam pipe. x coordinate points directly to the center of the LHC ring and y is

[1] The protons are injected from the CERN accelerator complex, containing for example accelerators Super Proton Synchrotron, Proton Synchrotron or PS Booster

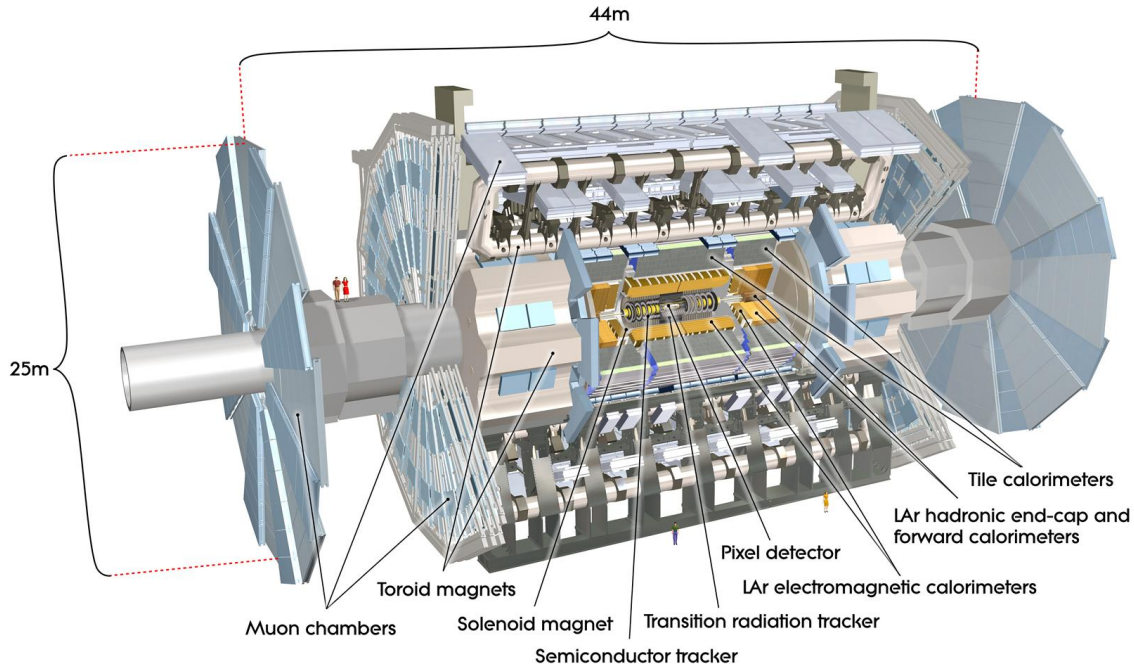

Figure 3.1: Overview of main parts of ATLAS - Inner Detector, Hadronic and Electromagnetic Calorimeters and Muon Detector, taken from [36].

perpendicular to both x, z and points upwards. However, the x, y, z coordinates are not commonly used and are replaced by cylindrical (or spherical) coordinates ϕ, r, z (ϕ, r, θ), where $\phi = 0$ points in direction of x axis (and θ=0 points along the z axis). Another important parameter is *pseudorapidity* η defined as $\eta = -\log \frac{\theta}{2}$ and *rapidity* y defined as $y = \frac{1}{2} \log \frac{E+p_z c}{E-p_z c}$. An advantage of rapidity is that it is additive under the Lorenz transformation, whereas pseudorapidity is easier to determine, since it only depends on angle θ. Both are equal for $m = 0$ and they are popular in particle physics, since distribution of particles is almost constant when expressed in terms of y, η. Sometimes, for simplifications, term forward (central) region will be used for high (low) values of $|\eta|$.

3.2.1 ATLAS triggers

The ATLAS computing would not be able to process and save all the collisions due to high rate of events. In order to reduced, there is large number of triggers implemented. They are set up in such way, that they focus on interesting events. One example can be the HLT_mu6 trigger (used later in this analysis), which fires when there is one muon with $p_T > 6$ GeV detected. The triggers are often prescaled, meaning only every n-th event is saved, in order to further reduce the event rate.

First level of trigger is purely hardware. A part of the detector serves as Level 1 (L1) trigger, which reduces maximal 40 MHz rate of events to only 75 kHz. It searches e.g. for high p_T leptons or jets. The event rate is further lowered by the high-level trigger (HLT) to optimal frequency 1kHz. In this analysis, only dimuon triggers are used, which require events with two leptons with some minimal transverse momentum.

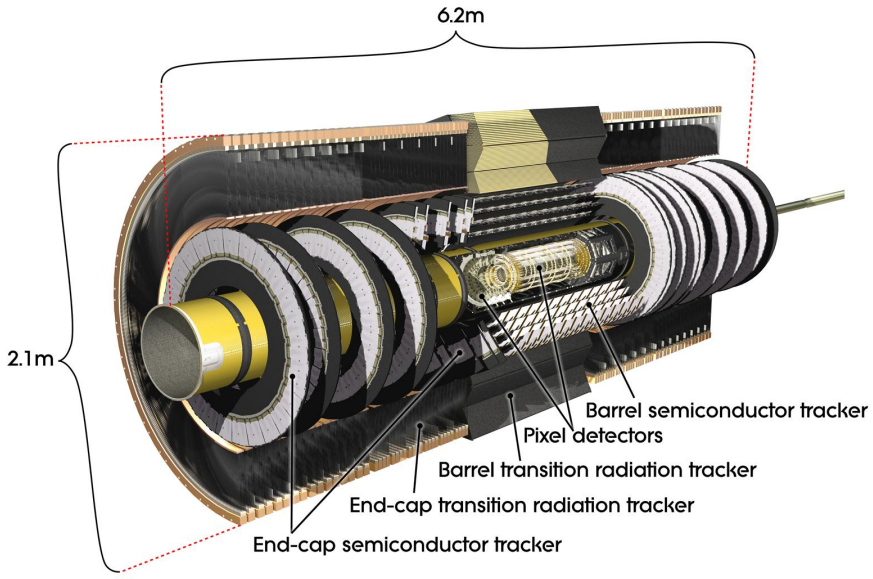

Figure 3.2: Overview of Inner Detector - barrel and end-cap, consisting of Pixel, SCT and TRT sub-detectors, copyright by **ATLAS Experiment ©2014 CERN** .

3.3 Inner detector

As can be seen in Figure 3.2, Inner Detector (ID) consists of three sub-detectors (Pixel, SCT and TRT) and two parts - barrel and end-caps. It is surrounded by a toroidal magnet with induction of 2T, which is shorter than the inner detector, resulting in a non-uniform field in the forward regions. Magnetic field causes deflection of charged particles in xy plane which is further used to determine p_T. The resolution of transverse momentum is $\frac{\Delta p_T}{p_T} = 0.04\% p_T + 2\%$, where p_T is in GeV.

Main purpose of the Inner Detector is a reconstruction of tracks - the trajectories of particles - and vertices - the points of either collision of particles or of their decays. In the case of the ATLAS, it is possible to reconstruct a particle with p_T as low as 100 MeV. However, in most cases minimal p_T of the reconstruction is set to 400 MeV, with an exception of e.g. minimum bias studies. In order to minimize energy loses and maximize efficiencies, material in the detector is minimized as much as possible [38]. ID covers whole ϕ region and $|\eta| < 2.5$.

Tracks are connected to another set of variables. Impact parameters define the distance of track's point of closest approach to the vertex. The ATLAS uses two - longitudinal z_0 coordinate, which is the distance alongside the z axis, and transverse impact parameter d_0, which is distance in the xy plane. Both definitions of impact parameters are illustrated in Figure 3.3. Transverse momentum p_T, part of momentum perpendicular to the z axis, is usually used instead of whole momentum, since it is invariant under Lorenz transformation and is directly determined from the curvature of particle trajectory. Another commonly used parameter is distance in ϕ, η plane: $R = \sqrt{\Delta\phi^2 + \Delta\eta^2}$, which is used for example in fitting of the tracks.

3.3.1 Pixel detector

Being closest to the beam and therefore to the collision, the pixel detector must have a large granularity to distinguish between large number of tracks and has to be able to resist great radiation. In R/ϕ it has resolution of 12 μm and in the z direction it has 110 μm [38]. The area of the detector is approximately 1.7 m^2 and it consists of three layers in both end-cap and barrel for Run 1. For Run 2, new layer -

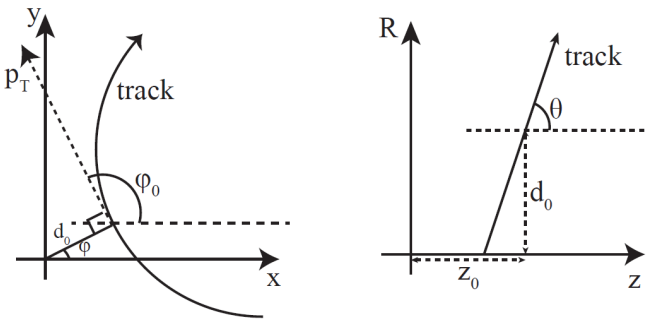

Figure 3.3: Definition of impact parameters d_0 and z_0, taken from [39].

Insertable Beam Layer (IBL) - is added. This layer is only 3.3 cm from the center of the detector and has full ϕ and $|\eta| < 2.5$ coverage. Basis of the Pixel detector are 1744 identical sensors, where each is composed of 47233 pixels. Most pixels have proportions 50×400 μm^2, only 10% are 50×600 μm^2. Optimal temperature is -7°C and voltage 600 V, but it is operational also at room temperature and with only 150 V [37]. In case of the IBL, the size of the pixels was reduced from 50×400 μm^2 to 50×250 μm^2 [40].

3.3.2 SCT detector

SCT (Semi Conductor Tracker) has a barrel and an end-cap, where barrel covers $|\eta| < 1.4$ and consists of four layers, end-caps cover $1.4 < |\eta| < 2.5$ and consists of nine layers on each side. There are 15912 silicon sensors, which operate on minimal voltage 150 V and optimal voltage 250-350 V [37]. Resolution is 9 μm [38].

Each layer consists of two back-to-back layers, which are necessary, since SCT is strip detector. In order to properly define hit, there needs to be signal in each layer and strips in those layers must not be parallel. There are two ways to approach this. They may be perpendicular, which ensures the most precise coordinates, but it may result in ghost hits. Other possibility, used in ATLAS, is to have a small angle between strips (in case of ATLAS it is $\approx 10°$), which leads to smaller precision, but lowers chance of false hits [39].

3.3.3 TRT detector

Transition Radiation Tracker (TRT) is the outer-most detector of the inner detector. Again, it consists of barrel ($|\eta| < 2$) and end-caps ($1 < |\eta| < 2.5$). Basic unit is a straw, which is parallel to the beam pipe for barrel and perpendicular for end-caps. This leads (for barrel) to good resolution in xy and consequently to poor resolution of z coordinate.

Straws of the TRT detector have a diameter of 4 mm and are composed of thin wire in gas (70% Xe, 27% CO_2, 3% O_2). The gas gets excited and ionized by passing particle. Due to electrical field, electrons and ions create a current, which can be measured. With this information, distance of the trajectory from the wire can be determined from the drift time.

TRT detector has also another function - it can distinguish between electrons and other particles. The space between straws is filled with a radiative material. When a particle passes the border of this material, X-rays are emitted (due to transition radiation, hence the name). Since this radiation is proportional to E/m, it is by far strongest for electrons. The emitted photons cause another excitation in the straws. For this reason, TRT has two thresholds, one for the measurement of passage of particle and one for the electron identification.

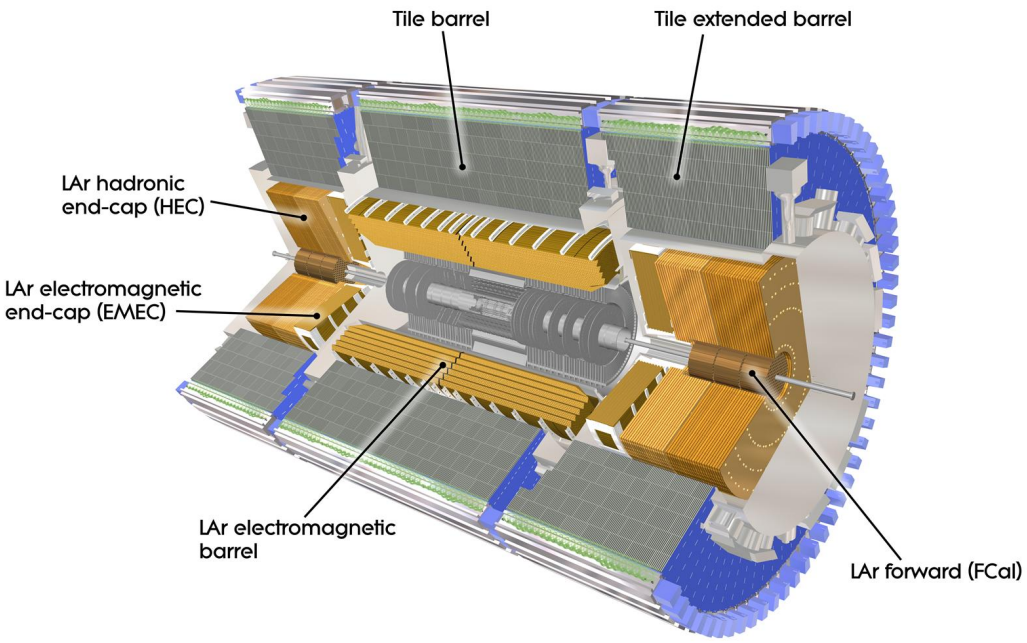

Figure 3.4: Schematic of the ATLAS calorimeter system, taken from [37].

3.4 Calorimeters

Calorimeters are used mainly to find out energy of particles by stopping them and measuring deposited energy. They usually have absorber part, which stops the particle, and sampling material, which measures the signal. The calorimeter system is displayed in figure 3.4. All information is taken from [37].

Electromagnetic calorimeter - main goal is to measure and identify the electrons and photons. It has lead absorber and liquid argon for sampling. It covers the whole ϕ region and is composed of a barrel and two end-caps with total coverage $|\eta| < 3.2$. The barrel is divided in two parts with a small gap in z=0. The detector has an accordion geometry which provides a full ϕ coverage.

In order to ensure most of the energy is contained within the EM calorimeter, its thickness is $>$ 22 radiation lengths[2] in the barrel and $>$ 24 in the end-caps. The resolution in energy is $\Delta E/E = 11.5\%/\sqrt{E} + 0.5\%$ and for ϕ, $\Delta\phi = 50/\sqrt{E}$ mrad, where in both cases energy is in GeV [38].

Hadronic calorimeter is placed around EM calorimeter and has 3 parts. First is the **Tile calorimeter**. It consists of a central barel ($|\eta| < 1$) and two extended barels ($0.8 < |\eta| < 1.7$). It uses a steel absorber and scintillator as sampling material. It has thickness of 9.7 interaction lengths[3]

Further there is a **LAr hadronic end-cap** placed behind the the EM calorimeter end-caps and covers $1.5 < |\eta| < 3.2$ and whole ϕ. Similarly to EM calorimeter, it uses liquid argon as sampling material, with copper as the absorber. The jet resolution of tile and hadronic end-cap calorimeter is $\Delta E/E = 50\%/\sqrt{E} + 3\%$, where E is in GeV[38].

Finally, the **LAr forward calorimeter** is placed around the beam pipe, covering angles up to $|\eta| = 4.9$. It is 10 interaction lengths long and has three moduls: first with copper absorber for electromagnetic measurement and two made of tungsten for hadrons.

[2]Radiation length is a distance on which electron or photon loses $1/e$ of its energy.
[3]Interaction length is, similarly to radiation length, a path after which hadron loses a $1/e$ of its energy.

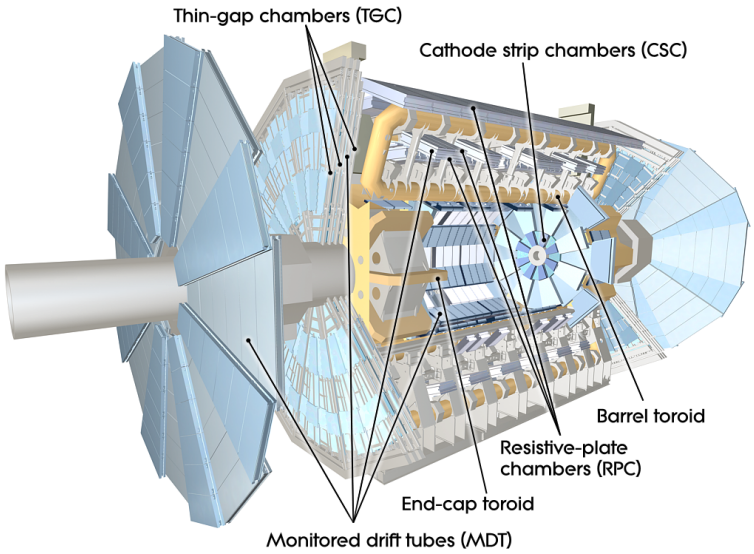

Figure 3.5: Schematic of the ATLAS muon system, taken from [37].

3.5 Muon spectrometer

As its name suggests, the muon spectrometer measures only muons (strictly speaking high p_T muons, which travel far enough to reach it). It consists of 3 barrel layers in 5, 7.5 and 10 meters from the beam pipe and 2×3 end-caps at $\pm 7.9, \pm 14, \pm 21.5$ meters, as can be seen in Figure 3.5. There is also the barrel toroid magnet for $|\eta| < 1.4$, while for $1.6 < |\eta| < 2.7$ there are two smaller end-cap magnets.

There are four sub-detectors in the muon spectrometer. The **Monitored Drift Tubes** (MDT) cover the whole η range and measure track coordinates. They are made of aluminum tubes of 30mm diameter with a cathode wire in the middle, where a position of the particle is determined from the drift time of the particle. Further there is **Cathode Strip Chamber** (CSC), a multiwire proportional chamber, which covers the most forward regions $2 < |\eta| < 2.7$ and is more radiation resistive and can therefore operate in a high radiation present near the beam pipe.

The trigger system consists of **Resistive Plate Chambers** (RPC), situated around the barrel, and **Thin Gap Chambers** (TGC), which are located in the end-cap regions. Together they cover $|\eta| < 2.4$. The RPC consists of two strip layers orthogonal to each other, with a gap between them filled with a gas. The TGC is a multi-wire proportional chamber with a quick drift time and is designed to provide a fast estimate of p_T of the muon.

3.6 Lepton measurement

Since the goal of the measurement is to measure two leptons in the final state, it is important to know, how they are identified by the ATLAS. Both electrons and muons are charged particles and therefore are detected by the inner detector.

3.6.1 Muons

Muons are the most penetrating particles and therefore pass trough both calorimeters and leave track in the muon spectrometer. Thus there are two tracks per muon, one in ID and one in MS. Based on the amount of information, there are four types of reconstructed muons in ATLAS. A stand-alone muon

is reconstructed only by the MS and can therefore also have $2.5 < |\eta| < 2.7$, out-side the ID coverage. The lowest background is found in combined muons, which are found by creating two independent tracks in the ID and MS and then combining them.

Sometimes, for example when it has a low p_T, the muon leave only a segment of a track in the SM. If a ID track can be extrapolated to the segment, than it is identified as a segment-tagged muon. Finally it is possible to identify a muon from ID track and the small amount of energy left behind in the calorimeter. Such muon is called calorimeter-tagged and has the biggest background[21]. In this analysis, the combined muons are used.

3.6.2 Electrons

Unlike the muons, electrons are usually stopped by the electromagnetic calorimeter, leaving behind a cluster. Such cluster can be also left by photon. It is a electron, when it can be connected with a track from the inner detector. Its energy is then determined from the energy deposited in the cluster, while the momentum and direction is determined from the ID information. Electrons have worse reconstruction efficiency than muons, because they suffer significant radiative losses.

Chapter 4

Strategy behind the current measurement

The diphoton processes have in comparison to the QCD interactions significantly smaller cross-section. Therefore it is not suprising that the exclusive processes make up only a small portion of the events with dilepton pair in the final state, the Drell-Yan process being predominant background. Numerous cuts have to be therefore applied in order to properly study the survival factor.

In this analysis only the muon pairs were considered, with possible expansion to electron pairs later. First, the general preselection of muon pairs will be discussed, which reduces fake muons and ensures clean sample. Then exclusive selection is explained, which significantly reduces background. Finally, various corrections applied are introduced.

4.1 Preselection

4.1.1 Muon selection

First, muons are required to pass the requirements of the Combined Muon, which was explained in the previous chapter. Specifically, there is requirement on the ID track:

- Number of pixel hits+number of crossed dead pixel sensors > 0
- Number of SCT hits+number of crossed dead SCT sensors > 4
- Number of pixel holes + number of SCT holes < 3.
- A successful TRT extension where expected

Furthermore, the muon has to have transverse momentum $p_T > 6$ GeV and $|\eta| < 2.4$, where the kinematic range is selected based on detector and trigger acceptance. In order to ensure the muon does not originate from a jet background, there is cut on d_0 significance, which is defined as $\frac{|d_0|}{\sigma_{d_0}}$ and has to be smaller than 3.

Finally, there is a isolation requirement in order to reduce multi-jet background, where sum of transverse momentum of additional particles in proximity of the muon has to be significantly smaller than the muon p_T. This is done by dedicated tool, which enables several modes of isolation.

4.1.2 Track selection

In order to select isolated muon pairs, the number of tracks in the proximity of the primary vertex needs to be determine. For this reason the track particles need to be properly defined. First, the

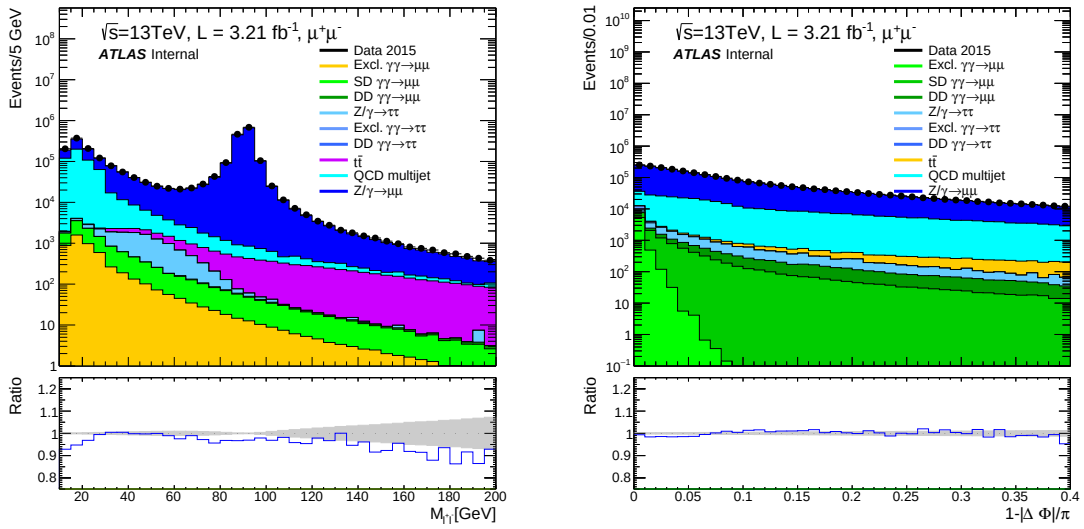

(a) (b)

Figure 4.1: (a) Invariant mass m_{ll} and (b) acoplanarity distributions after preselection.

two selected muons are excluded from the track definition. Furthermore, there is a cut on $p_T > 400$ MeV, which is a standard ATLAS p_T cut, since tracks with lower transverse momentum have small reconstruction efficiency.

Similarly to muon selection, there is a number of cuts on detector hits:

1. Number of silic hits >= 9 (11) if $|\eta| <= 1.65 (|\eta| > 1.65)$
2. Number of IBL hits + B-Layer hits > 0
3. Number of pixel hole = 0

4.1.3 Event selection

Since not all data acquired by the ATLAS are useful for an analysis, there is a preselection by requiring only events in so called Good Run List(GRL), which excludes e.g. events with parts of detector not functional.

For both Monte Carlo samples and data there is a requirement of several muon triggers, the basic one being trigger requiring two muons with $p_T > 10$ GeV (HLT), which is used for events with $m_{ll} > 30$ GeV. Further, dimuon triggers with $p_T > 6$ GeV were used to expand the kinematic region to lower values and are used for mass region $10 < m_{ll} < 30$ GeV. Trigger with $p_T > 4$ GeV, was also considered but its contribution was negligible and it was therefore omitted. Finally, two muons, as defined in section 4.1.1, with opposite charge are required. Those do not have to be necessarily the same muons identified with the triggers.

Distributions of data and all the considered MC are displayed in Figure 4.1. Aside from the fact that the Monte Carlos are in good correspondence with data, one can also notice a concentration of exclusive events in lower values of acoplanarity thanks to the fact that the two leptons are back-to back as expected. Also it is obvious the exclusive events form only negligible portion of the events and careful selection needs to be implemented in order to be able to determine the survival factor.

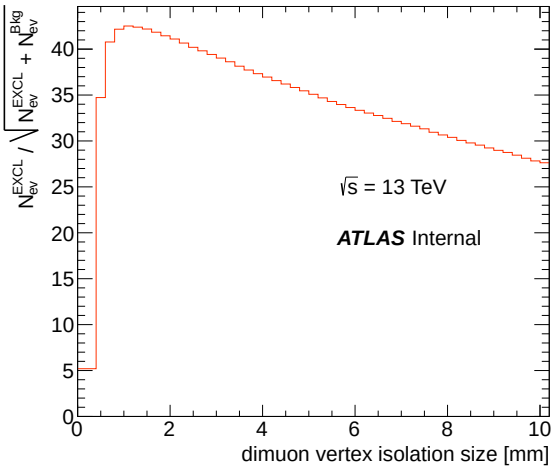

Figure 4.2: Dependence of the significance (as defined by Equation 4.1) on value of the Δz_0 cut. Courtesy to Mateusz Dyndal.

4.2 Exclusive selection

4.2.1 Dimuon vertex isolation

In contrast to the background processes, the exclusive dilepton production contains only two leptons in final state. Therefore first step in isolating the signal from the background is logically to require only two particles in the final state. However there are many collisions in one beam crossing on ATLAS and therefore additional particles are produced. Requiring events with only two muons would lead to practically zero yield.

This complication can be bypassed by concentrating only on a region around the dimuon vertex. This is done by requiring no additional particles in $\Delta z_0 < 1$ mm around the vertex. The value of the cut is determined from Monte Carlo by searching for best value of so-called significance:

$$significance = \frac{N_{ev}^{EXCL}}{\sqrt{N_{ev}^{tot}}}, \tag{4.1}$$

where N_{ev}^{EXCL} is number of exclusive events and N_{ev}^{tot} is total number of events. Dependence of this value on the Δz_0 cut can be found in Figure 4.2. Distribution of the events after the selection as function of m_{ll} can be found in Figure 4.3a). The fact that the Monte Carlo does not match data is caused by the absence of the survival factor. While on preselection level the photon processes were negligible and it did not have effect, it is significant on this level of selection.

4.2.2 Additional selection

Another useful property of the exclusive dilepton production is that the leptons are usually back-to-back. Therefore additional selection can be done by requiring cut either on transverse momentum of the dilepton system: $p_{T,ll} < 1.5$ GeV, or on acoplanarity $aco. = 1 - |\Delta\phi_{ll}|/\pi < 0.008$, which results in similar isolation of the signal, where the former one was taken in our case. The effect of this selection can be found in Figure 4.3b).

The background is now dominated only by the single-dissociative component, with exception of the Drell-Yan contribution in the Z mass region. It is therefore useful to exclude region $70 < m_{ll} < 105$ GeV from the events, making the Drell-Yan contribution negligible. The single dissociative component

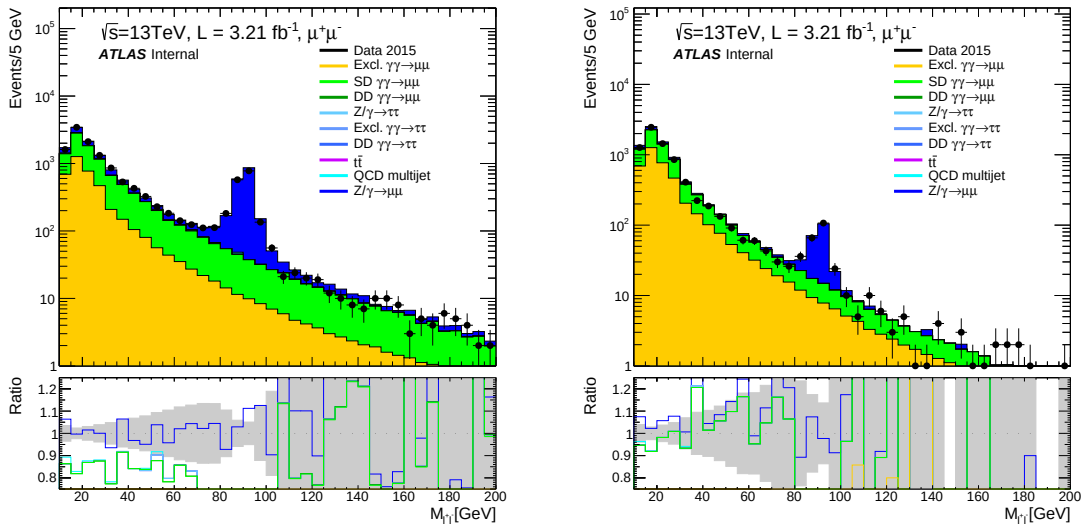

(a) (b)

Figure 4.3: Invariant mass m_{ll} and after (a) exclusive veto and (b) cut on $p_{T,ll}$.

is however non-reducible background. Most of the components of the proton dissociation are outside the kinematic range of the ATLAS detector and from the standpoint of the experiment is the SD identical to the exclusive component.

The number of events in all stages of selection process can be found Table 4.1.

Selection	Data	Signal	S-diss.	D-diss.	$Z\gamma/ \to \mu^+\mu^-$	QCD	$t\bar{t} \to \mu^+\mu^-$
Initial preselection	2933384	5605	8431	7667	2268000	590000	122000
1 mm exclusivity veto	14759	4451	6671	293	3900	50	0
Z region removed	12630	4351	6395	271	2000	50	0
$p_{T,\mu\mu} < 1.5$ GeV	8014	4291	3477	58	690	15	0

Table 4.1: Approximate number of events in the data and most of the Monte Carlo samples after all stages of selection process.

4.3 Correction to Monte Carlo

Precision of the deduced cross-section is directly connected to the ability to properly generate events and simulate their propagation through the detector. Various scale factors accounting for difference between data and Monte Carlo need to be applied. Example of this is scale factor for difference in track reconstruction efficiency, trigger efficiency, there is also smearing tool which corrects for modeling of impact parameter. Other correction is for mis-modeling of momentum resolution.

There are however still some corrections which had to be dedicated by analysis group. First, two examples of correction - Drell-Yan particle multiplicity and beam effects - will be presented, followed by more detailed description of derivation of trigger scale factor, where I contributed the most.

Drell-Yan particle multiplicity

The exclusive selection in essential at separating the Drell-Yan background. However as can be seen from Figure 4.4a), the particle multiplicity (dominated by the Drell-Yan sample) is mismodeled and in contrast to e.g. mass distribution it does not match the data. In order to correct this effect,

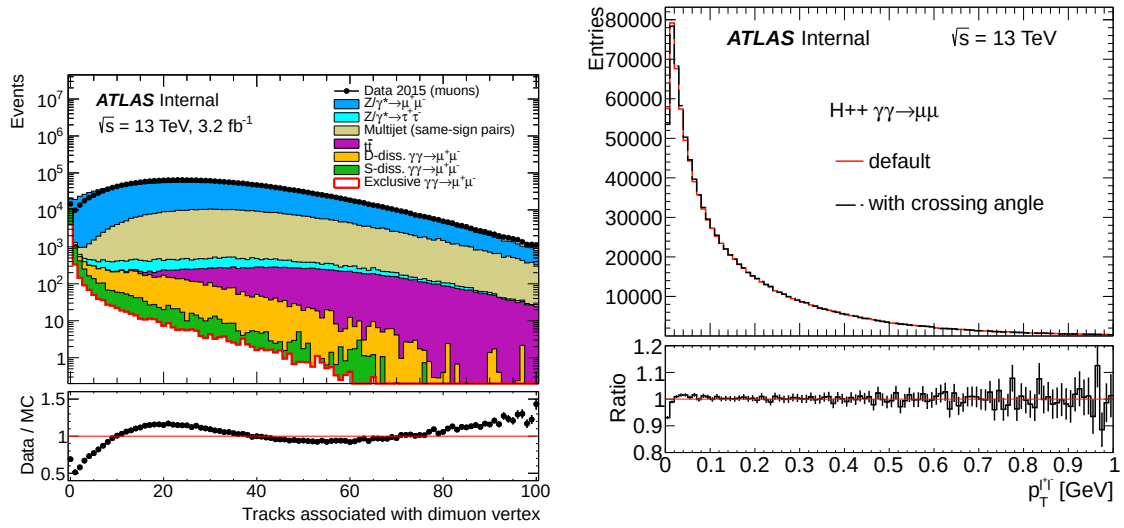

(a) (b)

Figure 4.4: (a) The track multiplicity on preselection level, (b) acoplanarity distribution with and without beam crossing angle correction. Courtesy to Mateusz Dyndal.

the data are unfolded[1] from reconstructed to particle level. Fraction of this truth level distribution of data and Monte Carlo is taken as a weight used on Monte Carlo.

Beam angle effect

In Monte Carlo proton beams are usually modeled as being parallel. In reality there is however a small angle between the beams, which leads to Lorentzian boost in y direction and change in the final results by 0.3% in previous analysis. Correction is done by simply applying Lorentzian Boost do the truth spectra. The impact of this correction is however small, as can be seen from Figure 4.4b).

4.3.1 Trigger scale-factor

Another significant difference between data and Monte Carlo is efficiency of triggers. While correction for the high p_T trigger was availabe, in case of the low$-p_T$ triggers the difference - scale factor - had to be derived.

Standard procedure is to determine efficiency of a muon being detected by the trigger $\epsilon_{matc,\mu}(p_T, q\eta)$ (where q is a charge of the muon) and trigger efficiency of a dimuon triggers is then defined as:

$$\epsilon_{trig,dimuon} = \epsilon_{match,\mu}(p_{T,1}, q_1\eta_1) \cdot \epsilon_{match,\mu}(p_{T,2}, q_2\eta_2) \cdot C$$

where C is correlation factor describing how the two muons affect each other. For muons separated by some significant distance this factor is simply 1. Since in this analysis the muons are back-to-back this is a reasonable approximation. The scale-factor, which later applied to data, is defined as a ratio of efficiencies for data and Monte Carlo.

For this study, a tool made by Dai Kobayashi was used (more information can be found in [42]) and the efficiency was derived for HLT_mu6 (which requires one muon with $p_T > 6GeV$). The tool uses a Tag&Probe method, which in order to minimize trigger bias and number of fake muons[2] uses decay products of some particle (usually Z boson or J/Ψ) and control trigger (e.g. HLT_mu4, which

[1] Bayesian unfolding is iterative method, which is used to determine original (truth) particle spectra from reconstructed distributions. More on this in reference [41].

[2] Where fake muon (or track in general) is muon not connected to any real particle, often reconstructed from random hits which incidently form a track.

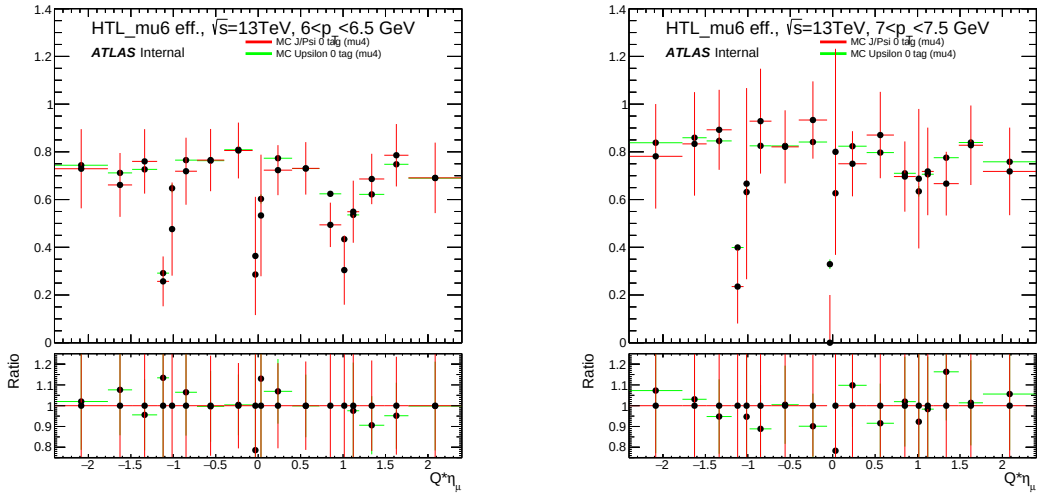

(a) (b)

Figure 4.5: Trigger efficiency of HLT_mu6 as function of η derived using Monte Carlo for (a) $6 < p_T < 6.5$ GeV and (b) $7 < p_T < 7.5$ GeV.

requires one muon with $p_T > 4GeV$). When the control trigger is fired, muon associated with it, called tag muon, is found. Next, all muons in event are combined with the tag muon and if their invariant mass is in some range around the studied parent particle, this second particle is taken as probe.

Next step is to find out, whether the probe muon corresponds to some trigger object of the studied trigger. The efficiency, taken as a function of muon p_T and $q\eta$, is then fraction of those matched probe muons and all probe muons. The whole process is slightly complicated by the fact that for large energies of the parent particle (e.g. J/ψ) the resulting muons are really close to each other and in order to eliminate correlation when information from both particles is overlayed (which is situation which will is not applicable to our analysis, where the muons are required to be almost back-to-back), a cut on distance $\Delta R = \sqrt{\Delta\eta^2 + \Delta\phi^2}$ is introduced.

In our case, the T&P method for employed for J/ψ and υ decays. The motivation for υ is that due to its bigger mass it is not that boosted for same values of p_T of the muons as for J/ψ and therefore there is not such problem with separation of the trigger objects. The efficiencies has to be the same for both parent particles, only with difference in number of events.

The method was employed for two types of tag triggers. First was already mentioned - the HLT_mu4 trigger - which gives the best statistics for Monte Carlo and therefore was used for it. Further there are two high p_T single muon triggers dedicated explicitly to J/ψ and υ triggering, which will be for simplicity labeled as $mu18$. This trigger is more useful in data, where the J/ψ or υ are more sparse.

Comparison of both parent particles for Monte Carlo can be found in Figure 4.5, while for data it is

The resulting efficiency Monte Carlo is in Figure 4.7a). Usage of several tag and probe methods serves as first validation of the efficiencies.

In order to validate the efficiency, closure test needs to be performed in the Monte Carlo. Finally, ratio of data- and MC-trigger efficiency gives the necessary scale factor, which can be found in figure 4.7b).

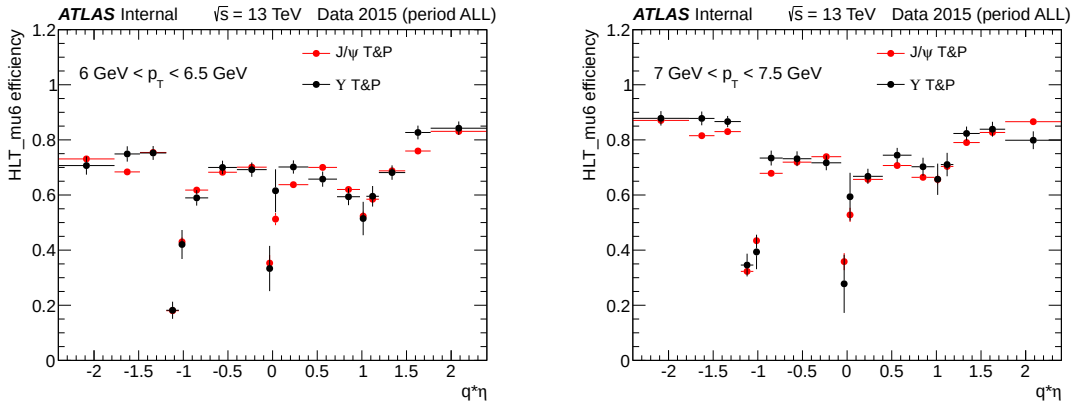

(a) (b)

Figure 4.6: Trigger efficiency of HLT_mu6 as function of η derived using data for (a) $6 < p_T < 6.5$ GeV and (b) $7 < p_T < 7.5$ GeV. Courtesy to Mateusz Dyndal.

Source	Variation from nominal yield
Muon reconstruction efficiency	1.3%
Muon momentum scale and resolution	0.3%
Muon trigger efficiency	3% (will be improved)
Pile-up description	0.5%
Exclusivity veto modelling	1.2%
Backgrounds	0.8%
LHC beam energy	0.4%
Template shapes	1.1%
Luminosity	2.1%
Total systematic uncertainty	4%
Statistical uncertainty	2.1%

Table 4.2: Summary of different contributions to the systematic uncertainty in the measurement. Courtesy to Mateusz Dyndal.

4.4 Systematic uncertainties

Detailed description of the systematic uncertainties is beyond the scope of this thesis. There is internal note being made which will include such description, but it will be available for members only. It is therefore appropriate to at least offer a short overview. The description is divided in two categories. First, muon-related systematics concerning for example the muon trigger efficiency. The secondy category summarizes the rest of the systematics.

All systematic uncertainties are determined by modifying the nominal distribution by changing one of the parameters - for example taking value of some efficiency modified by some factor (coming for example from statistical uncertainty). This way one gets set of modified distributions (usually there is one where the distribution is scaled up and one down). The difference between nominal and modified distribution is then summed in quadrature for each bin and square root is then taken as the systematic uncertainty.

All current systematic uncertainties are summarized in Table 4.2.

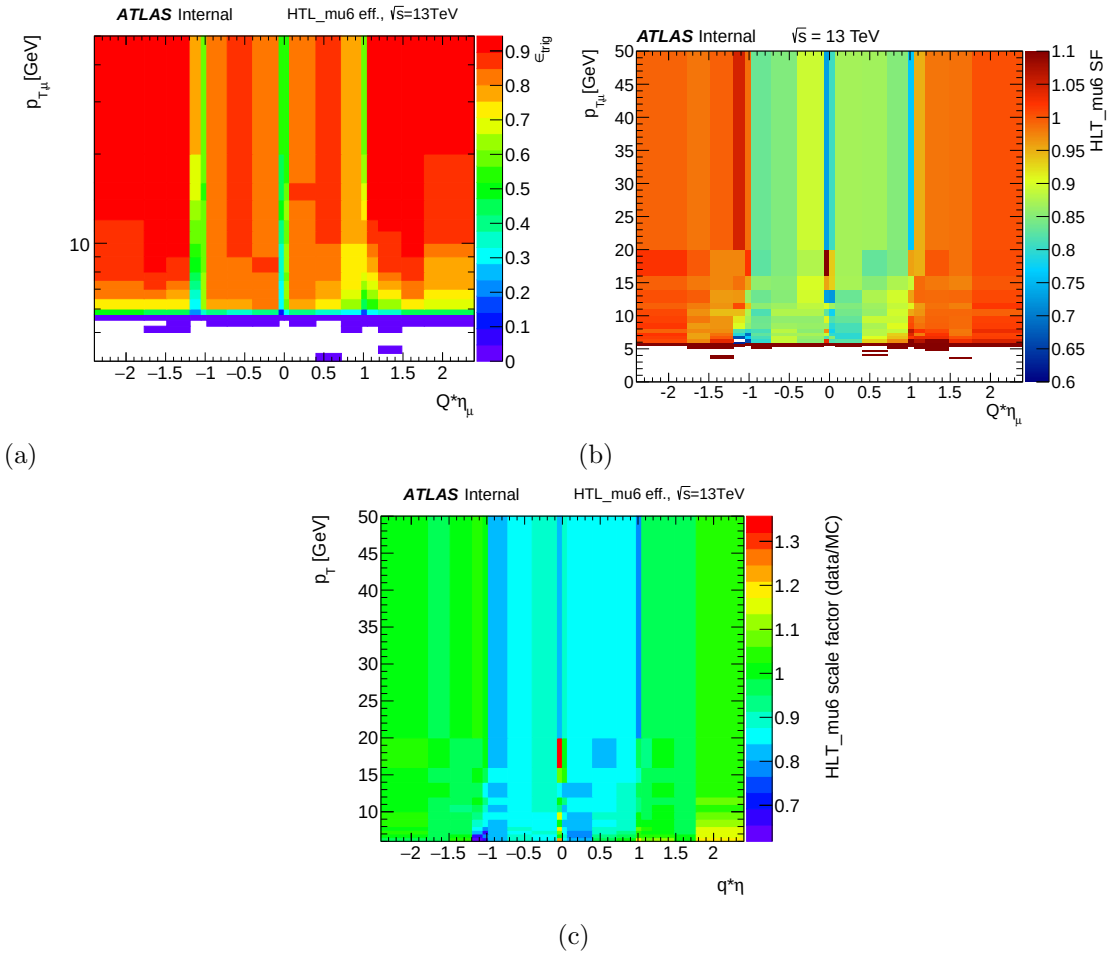

Figure 4.7: Trigger efficiency of *HLT_mu6* derived using (a) Monte Carlo, (b) data. (c) scale factor, taken as ratio of data and Monte Carlo trigger efficiencies.

4.4.1 Muon-related systematics

There are several systematics related to muons:

- **Reconstruction efficiency** - here the uncertainty comes from a statistical error of the scale factor. The nominal value is scaled up or down according to the uncertainty and thus one gets the UP and DOWN versions of the distribution. The total unc. is around 1.3%.

- **Momentum resolution and scale** - here are two separate uncertainties, one from the Inner Detector and one from the Muon Spectrometer, plus one uncertainty from momentum scale. Both resolution and scale uncertainties are found to be around 0.2%.

- **Trigger efficiency** uncertainty again comes from statistical uncertainty of the scale factor, whose derivation was described in previous section. Currently this uncertainty is dominant ($\approx$ 3%), however steps to significant reduction have been already taken (e.g. larger MC samples).

- **Isolation efficiency** is studied by using different mode of isolation and comparing the resulting distributions with nominal. The effect is however smaller than 0.2% and is considered negligible.

4.4.2 Additional systematics

- **Pile-up description** is studied using p_T, η distribution of pile-up particles far from the dimuon vertex. Ratio of such distribution for data and MC is then used to randomly add or remove tracks and effect on final distribution is studied. The effect is taken as systematic uncertainty and is found to be around 0.4 %.
- **Exclusivity veto efficiency** takes again difference between data and Monte Carlo in efficiency of the exclusivity veto. The effect is found to be 1.1%.
- **Background** uncertainty is determined differently for all background samples, but basic idea is to find how badly is the Monte Carlo simulated (by comparing data and MC or using different PDF set in simulation) and then considering effect on the final result. In total the uncertainty is 0.8%.
- **LHC beam energy** uncertainty was not studied for $E_{beam} = 6.5$ GeV, hence value from $E_{beam} = 4$ GeV is taken. The effect on final result is found to be 0.4%.
- **Template** is done by refitting with different acoplanarity template shapes and the uncertainty is around 1.1%.
- **Luminosity** uncertainty is produced by dedicated group and is found to be 2.1%.

Chapter 5

Fitting and results

As was mentioned before, the survival factor is found using a likelihood fit of the exclusive and single-dissociative components on data. First, a quick overview of the likelihood fit is presented, followed by description of error estimation. Then a practical implementation is described. Finally, method of systematic propagation is presented, together with a overview of systematic uncertainties.

5.1 Likelihood fit

Whole section is based on reference [43].

When some parameter α of a probability distribution $f(x, \alpha)$ is unknown (as for example normalization as in our case), it can be studied using a likelihood:

$$L(\alpha) = f(x = x_{data}, \alpha)$$

The estimator of the parameter α is such value of the parameter for which the likelihood is the biggest. For convenience a minus logarithm of the likelihood is often used and the minimum is required instead. Practically we then search for α_0, $\frac{\mathrm{d}L}{\mathrm{d}\alpha}|_{\alpha=\alpha_0} = 0$. The variance of the parameter can be estimated using Rao-Cramer-Frechet inequality leading to:

$$\sigma(\alpha) \approx \left(\frac{\mathrm{d}^2 \ln L}{\mathrm{d}\alpha^2} \right),$$

which can be interpreted as a value of σ for which $\ln L(p \pm \sigma) = \ln L_{min} - \frac{1}{2}$ when considering the Gauss distribution.

The maximal likelihood method has an advantage that it is unbiased for a large number of data points N (meaning $< \alpha >= \alpha_0$, where α_0 is true value of the parameter) and efficient ($< (\alpha - \alpha_0)^2 >$ is small for large N).

Disadvantage of the maximal likelihood is that its value does not hold any information about goodness-of-fit. In order to test the result of a fit, χ^2 test is usually used, where $\chi^2 = \sum_i \left(\frac{y_i - f(x,\alpha)}{\sigma_i} \right)$, where y_i is value of data measured at x_i. It can be shown that value of χ^2 approaches number of degrees of freedom N and probability follows distribution:

$$p(\chi^2, N) = \frac{2^{-N/2}}{\Gamma(N/2)} \chi^{N-2} \exp(-\chi^2/2).$$

The goodness of the fit can therefore be estimated by probability of resulting χ^2. Number of degrees of freedom when considering histogram is $N = N_{bins} - N_{param}$.

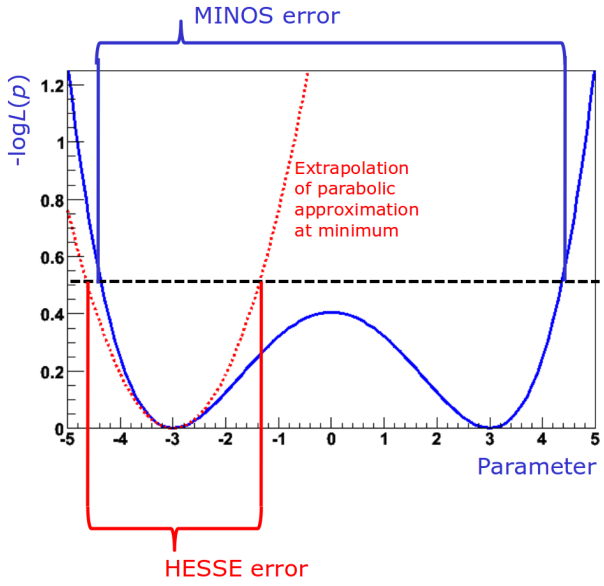

Figure 5.1: Comparison of error estimation through HESSE and MINOS errors. Taken from [44].

5.2 Practical implementation

5.2.1 MINUIT

MINUIT[46] is a common tool for likelihood or χ^2 fit used in High Energy Physics. Since most likelihood problems cannot be computed analytically, such tool is a necessity in order to perform numerical computation of the likelihood minimization. Since more local minimums can exist, it is useful and almost neccessary to estimate initial values of the parameters. This could in our case be result from previous analyses or theoretical prediction.

The MINUIT uses function **MIGRAD** to find the minimum. There are then two ways to estimate errors. First is **HESSE**, which produces symmetric errors through parabolic extrapolation at minimum and is based on the Rao-Cramer-Frechet inequality. The second method is **MINOS**, which searches for points where $\ln L(p \pm \sigma) = \ln L_{min} + \frac{1}{2}$. The second method is slower but more precise and can produced asymmetric error. Example of situation where this can lead to significant difference is in Figure 5.1. The tool also computes correlation coefficient and allows for multidimensional fits.

5.2.2 Survival factor fit

The survival factor was computed in ROOT[45] using a RooFit[47] package, which implements MINUIT. The survival factor concerns only the diphoton processes and it is already implemented into the double dissociative component. The fit is therefore done as a normalization fit of the exclusive and single-dissociative component. The fit is done in acoplanarity. The input distributions, fitted distributions and plot showing the best value and its errors can be found in Figure 5.2.

In order to check the results of fit, it was repeated for various fit regions for acoplanarity between 0 and 0.6. Those fits give similar results, mainly those with best χ^2 values tend to focus around value 90.8%. As a fit used in final results was used fit with χ^2/n closest to one. This fit leads to values

$$S^{excl} = 0.9086 + 0.0212 - 0.02104 \ (stat.)$$

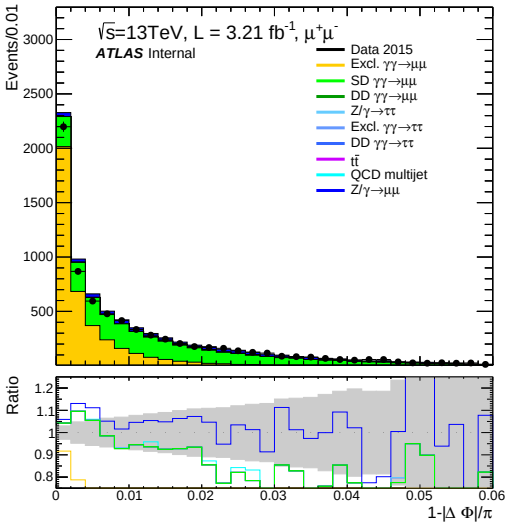

(1)

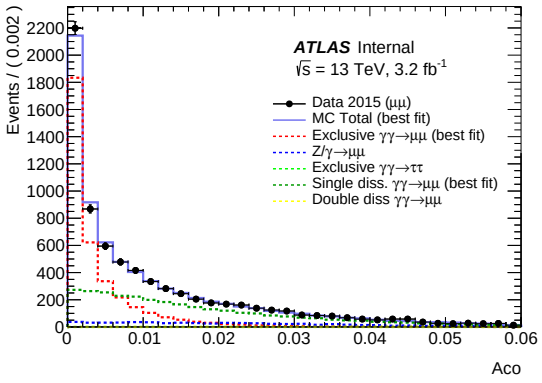

(2)

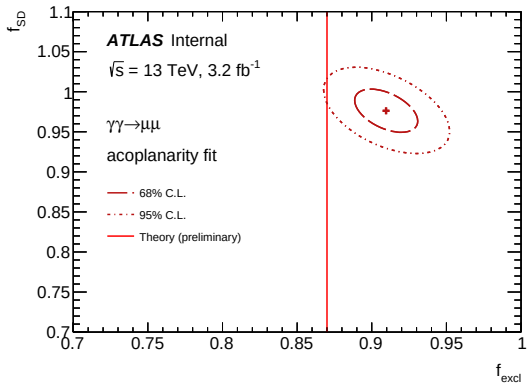

(3)

Figure 5.2: Figures depicting effect and results of the fit for the $p_{T,ll}$ cut: 1) The raw distributions before the fit, 2) Distributions with exclusive and single-dissociative component fitted to data, c) the value of best fit of fraction of the distributions together with a statistical error.

In order to study dependence of the impact parameter on various observables, fits in multiple slices of e.g. y_{ll} or m_{ll} are planned. Since this will lower the number of events used in fits, it will lead to less precise results, but will allow to study the survival factor in more detail (something what has no yet been done).

5.3 Results

The 2015 run at the LHC presents first opportunity for physicist to study collisions at record center-of-mass energies $\sqrt{s} = 13$ TeV. This means possible new physics, more precise results but at first determination of new efficiencies and corrections. Large number of studies are therefore repeated. On of them is the exclusive dilepton measurement.

The full sample from the new energies has integrated luminosity 3.21 fb^{-1} with uncertainty around 5%, comparable to statistic available at 7 TeV. However by inclusion of the low p_T muon triggers 3 times more events are observed, resulting in more precise results and possibility to study kinematic properties of the survival factor. It was also studied how many events are lost by the trigger requirement, but it was found to be smaller than 10%.

Total survival factor was measured by a likelihood fit currently only for the phase-space identified by the $p_{T,ll}$ cut, where the fit is done in acoplanarity. As was already mentioned, the survival factor was found to be:

$$S^{excl}_{p_{T,ll}} = 0.9086 + 0.0212 - 0.0210\ (stat.)$$

This result is optimistic since it is close to preliminary theoretical prediction (0.87 ± 0.02). The fit is also not significantly affected by choice of fitting region and the χ^2/N is found to be 0.9, close to the ideal value 1.

It can be therefore concluded that the analysis is heading in right direction. Preliminary results show that there will not be any large deviations from expected values. Further steps include for example the 2D fits.

5.3.1 Cross-section

The measured cross-section is defined in region divided in two kinematic sub-regions, where first is for invariant mass of the dilepton system 12 GeV $< m_{ll} <$ 30 GeV, with $p_{T,mu} > 6$ GeV, $|\eta| < 2.4$ and high mass region 12 GeV $< m_{ll}$, with $p_{T,mu} > 10$ GeV, $|\eta| < 2.4$. The p_T selection is mainly driven by the triggers, while the η is limited by geometry of the detector.

The cross-section for given fiducial region can be determined using following formula:

$$\sigma_{excl} = \frac{N_{obs} - N_{bkg}}{L_{int} \cdot \epsilon^{\mu\mu} \cdot \epsilon^{excl} \cdot c^{\mu\mu}}$$

where N_{obs} in number of observed events, N_{bkg} is number of background events (estimated from MC, both after application of survival factor), the L_{int} represents the integrated luminosity. $\epsilon^{\mu\mu}$ stands for efficiency of reconstruction of the dimuon pair and it accounts for muon reconstruction efficiency, trigger efficiency etc. The ϵ^{excl} accounts for reduction of events due to exclusive selection and $c^{\mu\mu}$ is the same but for the remaining selection (Z mass peak removal, $p_{T,ll} < 1.5$ GeV).

In our case those values are $L_{int} = 3.19 \pm 0.07$ fb^{-1}, $\epsilon^{\mu\mu} = 0395 \pm 0.013$, $\epsilon^{excl} = 0.794 \pm 0.012$, $c^{\mu\mu} = 0.964$, leading to cross-section:

$$\sigma_{excl} = 3.30 \pm 0.07(stat.) \pm 0.013(syst.)\texttt{pb}$$

5.3.2 Control plots

Control plots are used to check the survival factor by applying it to the Monte Carlo and checking how well are the additional distributions now described. In Figure 5.3 few such plots are shown, showing clearly good agreement between MC and data.

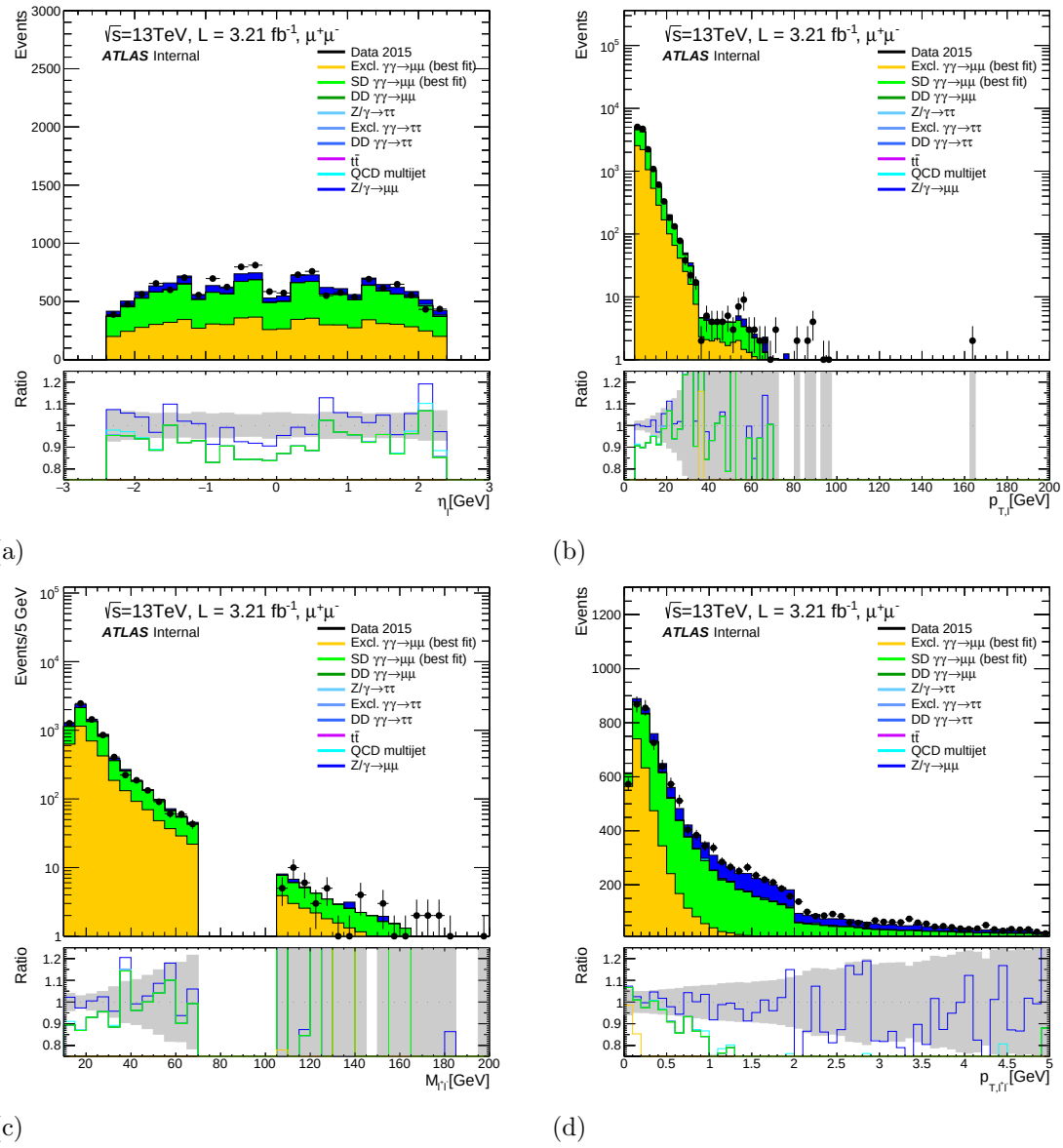

Figure 5.3: Control plots with MC corrected by survival factor, (a) for muon η,(b) for muon p_T, (c) for dimuon mass, all three after complete selection. (d) is for dimuon transverse momentum without the $p_{T,ll}$ cut.

Summary

Study of dilepton production and more importantly of the survival factor is important in order to study other, more rare, exclusive processes, as is for example light-by-light scattering or double W boson production. First, necessary theoretical background was presented in the first chapter, focusing on standard model and photon processes. This was followed in chapter two by description of equivalent photon approximation, which allows to study photon-photon processes in collisions of charged particles. It also reviewed previous measurements of the dilepton production and Monte Carlo used in the current analysis.

In the third chapter, the ATLAS detector is described in detail, together with a short description of the lepton reconstruction strategy. The details of the analysis, with focus on selection, are presented. This includes mainly requirement on no charged particle activity near the dilepton vertex and cut on dilepton transverse momentum. Currently the analysis is only for muon pairs, with possible inclusion of electrons in future. Further the corrections of Monte Carlo are presented, with focus on low$-p_T$ trigger scale factor. The fifth chapter is focused on derivation of the survival factor. First, likelihood fit is explained, together with software used to perform it.

Finally, at the end of the fifth chapter, current results are presented, where the total survival factor is found to be $S^{excl} = 0.9086 + 0.0212 - 0.0210$ $(stat.)$, value compatible with preliminary theoretical prediction $S^{theory} = 0.87 \pm 0.02$ $(theory)$. This leads to cross-section of exclusive dimuon production $\sigma_{excl} = 3.30 \pm 0.07(stat.) \pm 0.013(syst.)$pb.

Bibliography

[1] Michael Albrow and Emily Nurse, A search for exclusive Z→l events and a measurement of the $pp \to p\gamma\gamma p \to pllp$ cross section for dilepton invariant mass > 40 GeV/c^2,

http://www-cdf.fnal.gov/physics/new/qcd/exclZ_08/exclusive/

[Cited on 22. 2. 2016]

[2] nxhlh.com, Collision symmetry and measuring the asymmetry in the Drell-Yan process, http://www.nxhlh.com/collision-symmetry-and-measuring-the-asymmetry-in-the-drell-yan-process/

[Cited on 22. 2. 2016]

[3] Atlas Colaboration, Measurement of exclusive $\gamma\gamma \to l^+l^-$ production in proton-proton collisions at $\sqrt{s}$=7 TeV with the ATLAS detector, Phys.Lett. B749 (2015) 242-261

[4] Glenn F. Knoll, "Radiation Detection and Measurement," John Wiley & Sons, 16. 8. 2010

[5] L. Bergstrom, "Saas-Fee Lecture Notes: Multi-messenger Astronomy and Dark Matter," arXiv:1202.1170 [astro-ph.CO].

[6] Group Serra, Standard Model , http://www.physik.uzh.ch/groups/serra/StandardModel.html

[Cited on 7. 4. 2016]

[7] P. Achard *et al.* [L3 Collaboration], "Measurement of the running of the electromagnetic coupling at large momentum-transfer at LEP," Phys. Lett. B **623** (2005) 26 doi:10.1016/j.physletb.2005.07.052 [hep-ex/0507078].

[8] P. Skands, "Introduction to QCD," [arXiv:1207.2389 [hep-ph]].

[9] L. D. Landau and E. M. Lifschitz, "Production of electrons and positrons by a collision of two particles," Phys. Z. Sowjetunion **6** (1934) 244.

[10] S. J. Brodsky, T. Kinoshita and H. Terazawa, "Two Photon Mechanism of Particle Production by High-Energy Colliding Beams," Phys. Rev. D **4** (1971) 1532. doi:10.1103/PhysRevD.4.1532

[11] F. Krauss, M. Greiner and G. Soff, "Photon and gluon induced processes in relativistic heavy ion collisions," Prog. Part. Nucl. Phys. **39** (1997) 503. doi:10.1016/S0146-6410(97)00049-5

[12] A.I. Nikishov, "Absorption of High-Energy Photons in the Universe," JETP **14** (1962) 393.

[13] T. Piran, "The physics of gamma-ray bursts," Rev. Mod. Phys. **76** (2004) 1143 doi:10.1103/RevModPhys.76.1143 [astro-ph/0405503].

[14] A. Denner, S. Dittmaier and R. Schuster, "Radiative corrections to $\gamma\gamma \to W^+W^-$ in the electroweak standard model," Nucl. Phys. B **452** (1995) 80 doi:10.1016/0550-3213(95)00344-R [hep-ph/9503442].

[15] S. Chatrchyan *et al.* [CMS Collaboration], "Study of exclusive two-photon production of W^+W^- in pp collisions at $\sqrt{s} = 7$ TeV and constraints on anomalous quartic gauge couplings," JHEP **1307** (2013) 116 doi:10.1007/JHEP07(2013)116 [arXiv:1305.5596 [hep-ex]].

[16] D. d'Enterria and G. G. da Silveira, "Observing light-by-light scattering at the Large Hadron Collider," Phys. Rev. Lett. **111** (2013) 080405 Erratum: [Phys. Rev. Lett. **116** (2016) no.12, 129901] doi:10.1103/PhysRevLett.111.080405, 10.1103/PhysRevLett.116.129901 [arXiv:1305.7142 [hep-ph]].

[17] F. Moulin, D. Bernard and F. Amiranoff, "Photon-photon elastic scattering in the visible domain," Z. Phys. C **72** (1996) 607. doi:10.1007/s002880050282

[18] D. Bernard *et al.*, "Search for Stimulated Photon-Photon Scattering in Vacuum," Eur. Phys. J. D **10** (2000) 141 doi:10.1007/s100530050535 [arXiv:1007.0104 [physics.optics]].

[19] O. J. Pike, F. Mackenroth, E. G. Hill and S. J. Rose, "A photon–photon collider in a vacuum hohlraum," Nature Photon. **8** (2014) 434–436. doi:10.1038/nphoton.2014.95

[20] X. Ribeyre, M. Lobet, E. D'Humires, S. Jequier, V. T. Tikhonchuk and O. Jansen, "Pair creation in collision of γ-ray beams produced with high-intensity lasers," Phys. Rev. E **93** (2016) no.1, 013201 doi:10.1103/PhysRevE.93.013201 [arXiv:1504.07868 [physics.ins-det]].

[21] M. Dyndal, "Two-Photon Interactions in Proton−Proton Collisions with the ATLAS Experiment at the LHC," CERN-THESIS-2015-160.

[22] E. Fermi, "On the theory of collisions between atoms and electrically charged particles," Nuovo Cim. **2** (1925) 143 doi:10.1007/BF02961914 [hep-th/0205086].

[23] C. F. v. Weizsäcker, "Ausstrahlung bei Stößen sehr schneller Elektronen," Zeitschrift für Physik **88** (1934) 612

[24] E. J. Williams, Phys. Rev. **45** (1934) 729. doi:10.1103/PhysRev.45.729

[25] V. M. Budnev, I. F. Ginzburg, G. V. Meledin and V. G. Serbo, Nucl. Phys. B **63** (1973) 519. doi:10.1016/0550-3213(73)90162-4

[26] L. A. Harland-Lang, V. A. Khoze and M. G. Ryskin, JHEP **1603** (2016) 182 doi:10.1007/JHEP03(2016)182 [arXiv:1601.07187 [hep-ph]].

[27] L. A. Harland-Lang, V. A. Khoze and M. G. Ryskin, "The photon PDF in events with rapidity gaps," arXiv:1601.03772 [hep-ph].

[28] S. Chatrchyan *et al.* [CMS Collaboration], "Exclusive photon-photon production of muon pairs in proton-proton collisions at $\sqrt{s} = 7$ TeV," JHEP **1201** (2012) 052 doi:10.1007/JHEP01(2012)052 [arXiv:1111.5536 [hep-ex]].

[29] A. Abulencia *et al.* [CDF Collaboration], "Observation of Exclusive Electron-Positron Production in Hadron-Hadron Collisions," Phys. Rev. Lett. **98** (2007) 112001 doi:10.1103/PhysRevLett.98.112001 [hep-ex/0611040].

[30] T. Aaltonen *et al.* [CDF Collaboration], "Search for exclusive Z boson production and observation of high mass $p\bar{p} \to \gamma\gamma \to p + \ell\ell + \bar{p}$ events in $p\bar{p}$ collisions at $\sqrt{s} = 1.96$ TeV," Phys. Rev. Lett. **102** (2009) 222002 doi:10.1103/PhysRevLett.102.222002 [arXiv:0902.2816 [hep-ex]].

[31] T. Aaltonen *et al.* [CDF Collaboration], "Observation of exclusive charmonium production and $\gamma + \gamma$ to $\mu^+\mu^-$ in $p\bar{p}$ collisions at $\sqrt{s} = 1.96$ TeV," Phys. Rev. Lett. **102** (2009) 242001 doi:10.1103/PhysRevLett.102.242001 [arXiv:0902.1271 [hep-ex]].

[32] A. Aktas *et al.* [H1 Collaboration], "Muon pair production in ep collisions at HERA," Phys. Lett. B **583** (2004) 28 doi:10.1016/j.physletb.2004.01.003 [hep-ex/0311015].

[33] J. Adams *et al.* [STAR Collaboration], Phys. Rev. C **70** (2004) 031902 doi:10.1103/PhysRevC.70.031902 [nucl-ex/0404012].

[34] S. Afanasiev *et al.* [PHENIX Collaboration], "Photoproduction of J/psi and of high mass e+e- in ultra-peripheral Au+Au collisions at s**(1/2) = 200-GeV," Phys. Lett. B **679** (2009) 321 doi:10.1016/j.physletb.2009.07.061 [arXiv:0903.2041 [nucl-ex]].

[35] Stephen Myers, "The large hadron collider 2008–2013," Int. J. Mod. Phys. A, **28** (2013) 1330035 [DOI: 10.1142/S0217751X13300354].

[36] G. Aad *et al.* [ATLAS Collaboration], "Studies of the performance of the ATLAS detector using cosmic-ray muons," Eur. Phys. J. C **71** (2011) 1593 [arXiv:1011.6665 [physics.ins-det]].

[37] G. Aad *et al.* [ATLAS Collaboration], "The ATLAS Experiment at the CERN Large Hadron Collider," JINST **3** (2008) S08003.

[38] M. Limper, "Track and Vertex Reconstruction in the ATLAS Inner Detector," Amsterdam, Netherlands: Eigenverl. (2009).

[39] L. de Nooij, "The $\Phi(1020)$-meson production cross section measured with the ATLAS detector at $\sqrt{s} = 7$ TeV," CERN-THESIS-2014-035.

[40] Giordani, M, "Overview of the ATLAS Insertable B-Layer (IBL) Project," ATL-INDET-SLIDE-2012-428.

[41] Aaron Armbruster, Kevin Kröninger, Bogdan Malaescu, Francesco Spano, "Practical considerations for unfolding,"

[42] Dai Kobayashi, Summary of J/Ψ Tag&Probe,
https://drive.google.com/file/d/0B_ZLvkcWOdDnUTZia1l5dHRmSjQ/edit,
[Cited on 13. 5. 2016]

[43] Glen Cowan, "Statistical Data Analysis," Clarendon Press, 1998

[44] Wouter Verkerk, Parameter estimation χ^2 and likelihood (presentation),
https://www.physik.hu-berlin.de/de/gk1504/block-courses/autumn-2010/program_and_talks/Verkerke_part3,
[Cited on 21. 5. 2016]

[45] ROOT official website,
https://root.cern.ch/,
[Cited on 21. 5. 2016]

[46] MINUIT official website,
http://seal.web.cern.ch/seal/snapshot/work-packages/mathlibs/minuit/,
[Cited on 21. 5. 2016]

[47] RooFit official website,
http://roofit.sourceforge.net/,
[Cited on 21. 5. 2016]